



Coupled thermoacoustic interactions in hydrogen-enriched lean combustion

Abhishek Kushwaha^{1,2} · Amitesh Roy³ · Ianko Chtere⁴ · Isaac Boxx⁵ · R. I. Sujith^{1,2}

Received: 10 February 2024 / Revised: 19 June 2024 / Accepted: 22 June 2024 / Published online: 18 July 2024
© The Author(s), under exclusive licence to Springer-Verlag GmbH Germany, part of Springer Nature 2024

Abstract

In this paper, we apply a framework based on decomposition techniques to study the synchronization of flow velocity with acoustic pressure and heat release rate in swirl flames. The framework uses the extended proper orthogonal decomposition to identify regions of the velocity field where velocity and heat release fluctuations are highly correlated. We apply this framework to study coupled interactions associated with period-1 and period-2 type thermoacoustic instability in a technically premixed, swirl-stabilized gas turbine-type model combustor operated with hydrogen-enriched natural gas. We find the structures in the flame surface and the heat release rate correlated with the dominant coherent structures of the flow field using extended POD. We observe that the correlated structures in the flow velocity, flame surface and heat release rate fields share the same spatial regions during thermoacoustic instability with period-1 oscillations. In the case of period-2 oscillations, the structures from flame surface and heat release rate field are strongly correlated. However, these structures contribute less to the coherent structures of the flow field. Using the temporal coefficients of the dominant POD modes of the flow velocity field, we also observed 1:1 and 2:1 frequency locking behaviour among the time series of acoustic pressure, heat release rate and the temporal coefficients of the first two dominating POD modes of velocity field during the state of period-1 and period-2 oscillations, respectively. These frequency-locked states, which indicate the underlying phase-synchronization states, correlate with coherent structures in the flow velocity field.

1 Introduction

Reducing global greenhouse emissions is essential to ensure the habitability of our planet. One of the major sources of these emissions comes from the combustion of hydrocarbon fuels, which continues to be the primary source of power

generation in modern gas turbines utilized in aviation and thermal power plants. Lean combustion with the addition of hydrogen has become a significant alternative for enhancing lean combustion limits, providing high energy, and lowering carbon emissions (Janus et al. 1997; Hord 1978; Schefer 2003; Birol 2019).

Despite evident advantages, the effect of hydrogen enrichment on the thermoacoustic stability of turbulent combustors is not well understood and remains an active research topic.

Abhishek Kushwaha, Amitesh Roy, Isaac Boxx and R. I. Sujith contributed equally to this work.

✉ Abhishek Kushwaha
abhikushwaha8090@gmail.com

Amitesh Roy
amiteshroy94@yahoo.in

Ianko Chtere
ianko.chtere@gmail.com

Isaac Boxx
boxx@lom.rwth-aachen.de

R. I. Sujith
sujith@iitm.ac.in

² Centre of Excellence for Studying Critical Transition in Complex Systems, Organization, IIT Madras, Chennai, Tamil Nadu 600036, India

³ Institute for Aerospace Studies, University of Toronto, Toronto, ON M3H5T6, Canada

⁴ Institute for Combustion Technology, German Aerospace Centre (DLR), Stuttgart 70569, Germany

⁵ Chair of Optical Diagnostics for Energy, Process and Chemical Engineering, RWTH Aachen University, Street, Aachen 52062, Germany

¹ Department of Aerospace Engineering, IIT Madras, Chennai, Tamil Nadu 600036, India

Turbulent lean premixed flames are particularly sensitive to acoustic fluctuations. Under suitable conditions, the positive feedback among the acoustic field, turbulence and the flame leads to thermoacoustic instability, which results in large-amplitude pressure fluctuations (Lieuwen 2021; Sujith and Pawar 2021). Thermoacoustic instability (TAI) develops when heat release rate and pressure oscillations occur in-phase and the acoustic driving is greater than acoustic damping, leading to the energy increment to the acoustic field of the combustor (Rayleigh 1878; Chu 1965; Putnam 1971). The amplitude of pressure oscillations increases nonlinearities in the acoustic damping and the acoustic driving (Lieuwen and Yang 2005; Sujith and Pawar 2021). The balance between the acoustic losses and acoustic driving leads to limit cycle oscillations (Dowling 1997). The state of TAI can be detrimental to components of the engine, imparting structural damages, resulting in unscheduled shutdowns and mission failures (Juniper and Sujith 2018).

Large-scale coherent structures emerge during the onset of combustion instability in combustion systems (Poinot et al. 1987; Sterling and Zukoski 1987; George et al. 2018). The mutual synchronization of the reactive flow field with pressure oscillations is associated with the shift from stable combustor operation to the state of TAI (Mondal et al. 2017; Pawar et al. 2017; Singh et al. 2022). The goal of this study is to apply a new framework based on the extended POD for quantifying the synchronization of coherence structures in the flow with heat release rate and pressure oscillations in a swirl-stabilized combustor. To accomplish this, we quantify the mutual synchronization of these coherent flow structures with pressure oscillations during various dynamical states attained at various levels of hydrogen enrichment.

Swirling flames are used extensively in aircraft and gas turbine engines as they are one of the simplest and robust methods of stabilizing turbulent flame (Gupta et al. 1984; Hoffmann et al. 1994; Reddy et al. 2006; Freitag and Janicka 2007; Candel et al. 2014). The use of swirl flow leads to better air-fuel mixing (Syred et al. 2014), reduction in fuel consumption and decrease in exhaust pollutant emission (Rashwan et al. 2016).

Intense swirling flow gives rise to a central recirculation zone or a 'vortex breakdown bubble' (VBB) (Harvey 1962), which provides hot gases to the flame at the base, improving the static stability of the flame. The flow returns along the flow centre-line when the swirl number exceeds a critical threshold, forming an inner recirculation zone (IRZ) through helical instability (Gupta et al. 1984; Choi et al. 2007). The axial flux of azimuthal momentum divided by the axial flux of axial momentum is known as the swirl number. At sufficiently intense swirling conditions, precessing vortex cores (PVCs) form through helicoidal instabilities (Liang and Maxworthy 2005; Gallaire et al. 2006; Qadri et al. 2013). On the other hand, an outer recirculation zone (ORZ) is formed

when swirling flows encounter sudden expansion, leading to flow recirculation along the dump plane. Turbulent flames can stabilize either in the central recirculation zone (CRZ) or IRZ or in the ORZ or in both zones depending upon the overall geometry of the combustor (Gupta et al. 1984). Further, the hydrodynamic stability is altered significantly due to the presence of density stratification in non-isothermal conditions of turbulent flames. Indeed, density stratification has been shown to suppress the formation of PVCs (Oberleithner et al. 2013). Thus, the overall flow behaviour is strongly affected by the global stability of swirling flows and flames (Oberleithner et al. 2011; Stöhr et al. 2011).

Hydrogen enrichment can significantly alter the characteristics of turbulent flames. Comparing the size of the reaction zone to a pure methane-air flame stabilized by swirling, Wicksall et al. (2005) noticed that the addition of hydrogen to methane makes the flame more resilient. The increased concentration of OH, H, and O radicals in the ensuing H₂-enriched flame directly contributes to the increase in flame stability limits (Schefer 2003) in premixed turbulent combustors (Cozzi and Coghe 2006). One key feature of H₂-enrichment is the much higher burning velocity of the enriched methane mixture relative to pure methane due to the fast reaction rate of hydrogen observed in both numerical simulations (Hawkes and Chen 2004; Nam et al. 2019; Guo et al. 2020; Xia et al. 2022) and experiments (Mandilas et al. 2007; Strakey et al. 2007; Nakahara and Kido 2008; Zhang et al. 2020; Pignatelli et al. 2022).

Higher reaction rates also manifest in much larger increments in flame surface density upon H₂-enrichment (Halter et al. 2007; Guo et al. 2010) and enhancement of flame wrinkling due to interactions of small scales of turbulence with the flame front (Emadi et al. 2012). Further, the addition of hydrogen alters the manner in which the flame interacts with turbulence and pressure fluctuations, thereby leading to an increased rate of reaction of hydrogen-blended methane (Kim et al. 2009). The addition of H₂ enhances flame anchoring and lean combustion limits by strengthening the flame's resistance to strain brought on by turbulence (Schefer et al. 2002; Zhang et al. 2011).

As such, H₂ enrichment in methane increases the flame surface area and the flame wrinkling and also contributes to the state of TAI by increasing the heat release rate fluctuations (Zhang and Ratner 2019). Moreover, the overall change in the flame shape at various levels of H₂-enrichment is also a strong contributor to TAI while affecting pollutant emissions (Schmitt et al. 2007). Tuncer et al. (2009) reported that a shift in the flame centre of mass towards the inlet, due to an increase in the burning velocity with hydrogen enrichment, controls the shape of the flame. Similarly, swirling methane-air flame under different levels of H₂ enrichment undergoes drastic change from columnar, V-shape to M-shape flame (Davis et al. 2013; Taamallah

et al. 2015; Shanbhogue et al. 2016; Chterev and Boxx 2019). In fact, these effects persist at elevated pressures at various levels of H_2 enrichment (Chterev and Boxx 2021), which determine the exact flame shape depending upon the stability of the swirling flow. García-Armingol et al. (2014) found that a V-flame transitions to an M-flame whenever the swirling flow features an outer reaction zone.

Using linear stability analysis, Oberleithner et al. (2015) showed that V-shape flames possess strong radial density/temperature gradients, thus suppressing the formation of precessing vortex cores (PVC) and the flame predominantly anchors along the shear layer. In contrast, M-flames anchor along the outer recirculation zones and possess smooth density gradients. These flames also exhibit PVCs. However, the role of PVCs in driving thermoacoustic instabilities has not yet been resolved satisfactorily (Candel et al. 2014). While initially thought to be a contributor of thermoacoustic instability (Gupta et al. 1984; Huang and Yang 2009), in many cases PVCs have been found to have limited impact on the thermoacoustic characteristics of axisymmetric swirl combustors (Boxx et al. 2010; Moeck and Paschereit 2012; Oberleithner et al. 2013). This is due to PVC-induced anti-symmetric flame perturbations, which have no impact on oscillations in the global heat release rate (Candel et al. 2014).

In the specific context of thermoacoustic instability in swirl combustors, the addition of H_2 can shift the state to TAI from combustion noise (Janus et al. 1997). Here, the term “combustion noise” refers to a steady operating condition characterized by low amplitude aperiodic acoustic oscillations with broadband spectra (Candel et al. 2009) and fractal characteristics (Nair and Sujith 2014). The addition of hydrogen shifts the occurrence of the state of TAI (Figura et al. 2007) to lower equivalence ratios accompanied by a reduction in dynamic pressure amplitude. These characteristics were ascribed to the hydrogen present in the combination of CH_4 and H_2 , which caused a higher rate of reaction and a shorter convective time scale. Hong et al. (2013) reported a varying frequency and flame response when hydrogen was varied as a result of a change in the relative phase between heat release rate and pressure fluctuations. In addition to seeing several developments related to the flame transfer function, Æsøy et al. (2020) showed a reduction in the phase difference between heat release rate and pressure for hydrogen-enriched fuel. Lee and Kim (2020) separately investigated the dynamics of a mesoscale burner for the combustion of methane and hydrogen and reported that the dynamics are connected with higher eigenmodes for pure hydrogen operation. Similarly, many research studies show different effects of hydrogen enrichment on the combustion dynamics (Taamallah et al. 2015; Shanbhogue et al. 2016; Zhang and Ratner 2019; Chterev and Boxx 2019).

Coherent structures are intimately related to the overall thermoacoustic behaviour of turbulent combustors (Poinsot et al. 1987; Sterling and Zukoski 1987; Schadow and Gutmark 1992) as these structures dictate the behaviour of the flow. Using techniques such as spark-Schlieren imaging and C_2 radiation mapping, these studies tracked the formation, growth and decay of coherent structures. These structures affect the mixing process of the unburnt fuel-air mixture with burnt hot gases. The mutual synchronization of the pressure fluctuations with the periodic shedding of coherent structures is one of the key mechanisms underlying the emergence of the state of TAI (Poinsot et al. 1987; Pawar et al. 2017; George et al. 2018).

One of the most significant techniques for analysing coherent patterns in turbulent flow is the proper orthogonal decomposition (POD) approach (Lumley 1967; Sirovich 1987). POD method reduces the description of turbulent flow fields in terms of orthogonal modes, which are obtained by optimizing the L^2 -norm or the kinetic energy of the velocity field. The POD modes are orthogonal and characterize the most energy-containing coherent structures. Fluid dynamical systems have strongly coupled subsystems, and to understand the effect of coherent structures in the flow on other correlated variables, Borée (2003) introduced the extended proper orthogonal decomposition (EPOD). The method is used to project other correlated variables, such as concentration and temperature, on the POD modes of the velocity field and obtain analogous flow structures in such correlated variables. Using EPOD, Wang et al. (2018) showed the coupling between pressure and velocity by analysing the overlapping of the structures from the aforementioned fields in flow instabilities numerically.

In the context of thermoacoustics, the relationship between coherent structures and pressure variations has been investigated using POD. For instance, Sui et al. (2017) used the POD method to understand the behaviour of acoustic fluctuations of different eigenmodes in space using the reconstructed 2-D acoustic pressure field of a Rijke tube. They reported that the heating source mitigates the pressure fluctuations. They also showed 1:1 and 2:1 coupling among different filtered modal coefficients using the traditional Lissajous patterns (axisymmetric patterns). The Lissajous pattern is the representation method for a pair of signals by which the frequency locking behaviour can be provided in terms of the ratio between the dominating frequencies of the pair of signals (Greenslade Jr 1993). Boxx et al. (2010) used POD to study the PVC and showed that the dominant vortices in the most energetic mode rotate in the counter-clockwise direction. However, the second mode has the dominating vortices rotating clockwise. With the help of POD modes, they reported that the first two dominating modes represent a helical PVC and the third mode is associated with the thermoacoustic pulsation in the axial

direction. Duwig and Iudiciani (2010) used EPOD to study the correlation among the modes of the reacting flow field and the unsteady flame using PLIF data for the acoustically excited flame. Similarly, EPOD has also been used to determine the effect of coherent structures on correlated modes of related variables such as pressure, temperature, and scalar concentrations (OH^* and CH^* intensity fields) in various thermoacoustic systems (Sieber et al. 2017; Wang et al. 2019; Lohrasbi et al. 2021).

In this study, we aim to apply a framework based on decomposition techniques to understand the synchronization of the flow velocity field with heat release rate and acoustic pressure and to clarify the manner in which the addition of H_2 affects coherent flow structures of a highly turbulent swirling flame, influence heat release rate fluctuations and modify the thermoacoustic behaviour in a partially premixed, swirl-stabilized flame. To characterize the coupled interaction, we use POD to obtain the dominant modes of the measured velocity field. We unravel their effect on the heat release rate fluctuations through the use of EPOD modes. This also enables us to correlate how the thermoacoustic behaviour is affected by the addition of H_2 . We compare the behaviour of such extended POD modes during the state of period-1 (a single dominant frequency) and period-2 (two dominant frequency) thermoacoustic instability (Kushwaha et al. 2021) and contrast their characteristics with the baseline case of combustion noise. By analysing the spatial

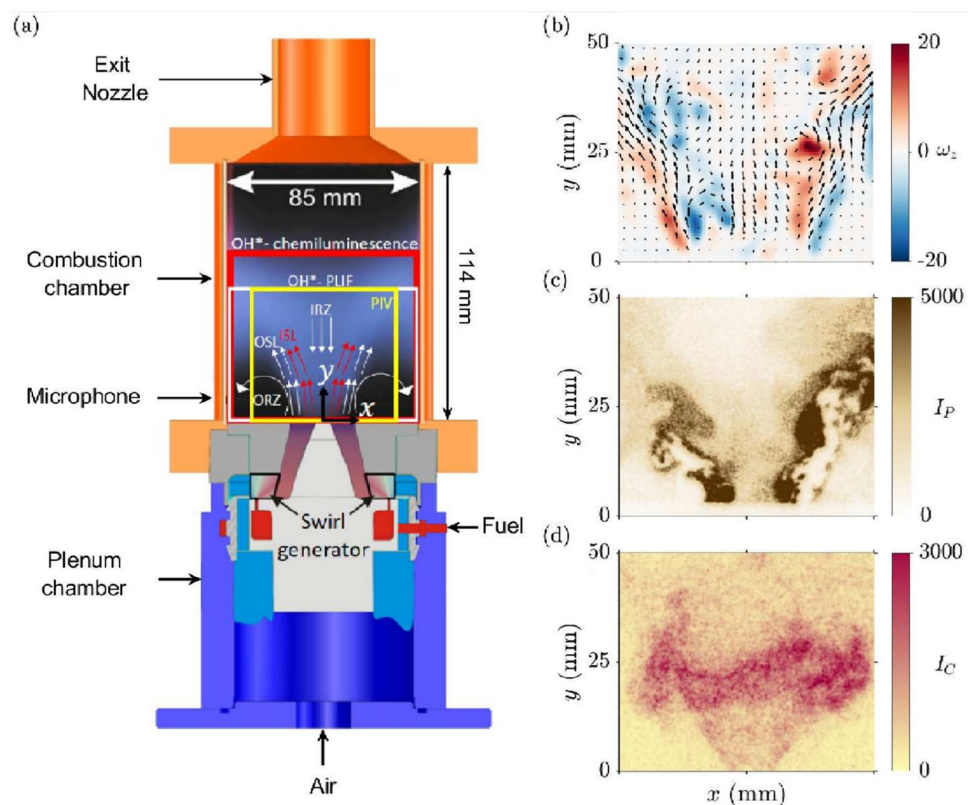
EPOD modes simultaneously, we relate the behaviour of the dominant modes of the swirling flow, the flame structure and the heat release rate field with the self-excited acoustic mode of the combustor. In this manner, we delineate the overall synchronization behaviour of the swirling flames during various dynamical states and relate them to the dominant modes or the coherent structure of the swirling flow.

The rest of the paper is organized as follows. In Sect. 2, the details of the experimental set-up and the imaging techniques used are provided. In Sect. 3, we discuss the methodology used for characterizing the coupled interactions and check the existence of the chaos. This is followed by results and discussion in Sect. 4. We summarize our major findings in Sect. 5.

2 Experimental setup

The experiments were performed at atmospheric pressure in the technically premixed gas turbine model combustor (PRECCINSTA configuration) shown in Fig. 1 of the manuscript. Air enters the cylindrical plenum before passing through a swirl generator with 12 radial swirl channels. Fuel (methane with variable quantities of hydrogen addition) is injected into each swirl channel through a 1 mm aperture. Through a conical nozzle with an exit diameter ($D = 27.85$ mm), the partially premixed swirling reactant flow

Fig. 1 (a) Schematic of the swirl-stabilized PRECCINSTA combustor. Various features of the swirling flow are identified: *OSL* outer shear layer, *ISL* inner shear layer, *ORZ* outer recirculation zone and *IRZ* inner recirculation zone. The domain of particle image velocimetry (PIV), OH^* -chemiluminescence and planar laser-induced fluorescence (PLIF) imaging are also indicated (Kushwaha et al. 2021). Instantaneous (b) vorticity field, (c) OH -PLIF intensity showing the flame area, and (d) OH^* -chemiluminescence field showing the heat release rate distribution are also shown for reference



reaches the combustion chamber. The chamber has a height of 114 mm and a square cross-sectional area of $85 \times 85 \text{ mm}^2$. Metal brackets at the corner are used for supporting quartz glass to give optical access to the combustion chamber. The exit of the combustor consists of a conical nozzle followed with an exhaust duct. The contraction ratio (ratio of the area of the exit of the nozzle at the inlet of the combustor to the cross-sectional area of the combustion chamber) is 0.17. This contraction ratio ensures combustion at atmospheric pressure inside the combustion chamber.

Three separate mass flow sensing meters are used to control the mass flow rate of methane (\dot{m}_{CH_4}), hydrogen (\dot{m}_{H_2}) and air (\dot{m}_a). The addition of hydrogen with methane is done in such a way that the global equivalence ratio (ϕ_g) and thermal power (P_{th}) remain constant for each case. These operating conditions are obtained by simultaneously decreasing \dot{m}_{CH_4} and increasing \dot{m}_{H_2} . The thermal power for the combustor is measured using $P_{th} = \dot{m}_{\text{CH}_4} h_{\text{CH}_4} + \dot{m}_{\text{H}_2} h_{\text{H}_2}$, where h_{CH_4} and h_{H_2} are the calorific values of methane ($h_{\text{CH}_4} = 55.5 \text{ MJ/kg}$) and hydrogen ($h_{\text{H}_2} = 141.7 \text{ MJ/kg}$), respectively. The thermal power P_{th} for the experiments varies from 22.17 kW to 25.31 kW as the volumetric percentage of H_2 varies. The nominal Reynolds number Re for the experiments is calculated using the expression,

$$Re = \frac{4\dot{m}_t}{\mu\pi L_c} \tag{1}$$

where $\dot{m}_t (= \dot{m}_{\text{CH}_4} + \dot{m}_{\text{H}_2} + \dot{m}_a)$ denotes the total mass flow rate in kg/s. The value of the dynamic viscosity (μ) for the mixture of $\text{H}_2 - \text{CH}_4$ -air is computed according to Wilke (1950). The diameter (D) of the nozzle at the inlet of the combustion chamber is used as the characteristic length (L_c). Re ranges from 2.3×10^4 to 2.8×10^4 . The global equivalence ratio (ϕ_g), the thermal power (P_{th}) and the Reynolds number (Re) are listed in Table 1.

Various measurements were performed to understand the state of the system. To measure acoustic pressure fluctuations in the combustion chamber associated with different dynamical states, amplitude and phase-calibrated microphone probe with a Brüel and Kjaer (B&K) Type 4939 1/4-inch Free-field condenser microphone was used. The sensitivity of the microphone is 4 mV/Pa, and the uncertainty

is $\pm 3 \text{ dB}$. The microphone was positioned 20 mm from the dump plane of the combustor and recorded data at a sampling frequency of 100 kHz.

Stereoscopic particle image velocimetry (sPIV) is used to measure the flow characteristics inside the combustor. A dual-cavity, diode-pumped solid-state laser (Edgewave, IS200-2-LD, up to 9 mJ/pulse at 532 nm) and a pair of CMOS cameras (Phantom v1212) positioned on the opposite sides of the laser sheet, looking down into the combustor, make up the stereo-PIV system. 10,000 (1 s) PIV images are acquired at a resolution of 640×800 pixels for each operational state. The PIV measurement domain spans a region of $65 \times 50 \text{ mm}^2$, ($-32 < x < 32 \text{ mm}$ and $0 < y < 50 \text{ mm}$ in Fig. 1). The projected pixel resolution of the PIV system is 0.08 mm/pixel. The inter-frame pulse separation (Δt) is set to 10 ms. A pair of cylindrical lenses ($f = -38 \text{ mm}$ and 250 mm) are used to shape the beam into a sheet, and a third cylindrical lens ($f = 700 \text{ mm}$) is used to thin it to a waist. Titanium dioxide (TiO_2) particles with a nominal diameter of $1 \mu\text{m}$ are seeded into the airflow inside the combustor to obtain the scattered fluorescence. A commercial, multi-pass adaptive window offset cross-correlation technique is used to accomplish image mapping, calibration, and particle cross-correlations (LaVision DaVis 10). The final interrogation window size is 16×16 pixels with a 50% overlap. This corresponds to a window size of 1.3 mm and vector spacing of 0.65 mm. In this manner, the three components of velocity in a plane aligned with the burner centre-line are quantified. Based on the correlation statistics in LaVision DaVis, the uncertainty in the instantaneous velocities is estimated to be $\pm 0.7 \text{ m/s}$ for the in-plane components (x - y) and $\pm 1.8 \text{ m/s}$ for the out-of-plane component (z -axis). Figure 1b shows a typical instance of the velocity field obtained from the PIV measurements. In this study, we are referring the x -component of the velocity (u_x), acquired in the Cartesian frame of reference as the transverse component and the y -component of the velocity (u_y) as the axial component of the flow field.

An intensified high-speed CMOS camera (LaVision HSS 5 with LaVision HS-IRO) equipped with a fast UV objective lens (Halle, $f = 64 \text{ mm}$, $f/2.0$) and a bandpass filter (300-325 nm) is used to image the line of sight integrated chemiluminescence from the self-excited OH^* radical over a 512×512 pixel resolution. Depending on the signal intensity, the

Table 1 The values of different operating parameters during the experiments. Keys: $\text{H}_2(\%)$ -Volumetric percentage of H_2 in the fuel; Re -Nominal Reynolds number; ϕ_g -Global equivalence ratio; P_{th} -Thermal power rating (kW) and dynamical states

Sr. No	$\text{H}_2(\%)$	$Re(\times 10^4)$	ϕ_g	P_{th} (kW)	p'_{rms} (kPa)	Dynamical state
1	0	2.41	0.65	25.31	0.09	Chaotic
2	20	2.74	0.65	22.26	0.91	P2 LCO
3	50	2.64	0.65	22.50	0.71	P1 LCO

intensifier gate time is ranged from 25 to 50 μ s. The number of images for each recording is limited by the onboard memory of the camera. For each condition, 8192 frames were captured. The global heat release rate $\dot{q}'(t)$ signal is calculated by integrating the intensity of all pixels.

The OH-planar laser-induced fluorescence (PLIF) imaging system consists of a frequency-doubled dye laser pumped by a high-speed, pulsed Nd:YAG laser (Edgewave IS400-2-L, 150 W at 532 nm and 10 kHz) and an intensified high-speed CMOS camera system. The dye laser system (Sirah Credo) was operated in the range of 5.3 W to 5.5 W at 283 nm with a repetition rate of 10 kHz (i.e. 0.53 – 0.55 mJ/pulse). The dye laser was tuned to excite the $Q_1(6)$ line of the $A^2 \Sigma^+ - X^2 \Pi$ ($v'=1, v''=0$) band. A photo-multiplier tube (PMT) with WG-305 and UG-11 filters and a reference laminar premixed flame were used to continually monitor the laser wavelength during the experiments. The 283 nm PLIF excitation beam is formed into a sheet approximately 50 mm high \times 0.2 mm thick using three fused-silica, cylindrical lenses. All the lenses are coated with anti-reflective coating to maximize transmission.

A high-speed CMOS camera (LaVision HSS 6) and an external two-stage intensifier (LaVision HS-IRO) positioned on the other side of the combustor from the OH camera are used to image the OH-PLIF fluorescence signal. Another fast UV objective lens (Cercor, $f=45$ mm, $f/1.8$) and a bandpass filter (300-325 nm) are fitted to the OH-PLIF camera. With an array size of 768×768 pixels, the camera's projected pixel resolution was 0.115 mm/pixel. OH*-chemiluminescence, OH-PLIF, and stereo-PIV images were acquired simultaneously at a sampling frequency of 10 kHz and were phase-locked to the microphone measurements sampling data at 100 kHz. In this study, we have used only the common regions covered by all three imaging techniques.

3 Method of analysis

3.1 Extended proper orthogonal decomposition for obtaining correlated flow structures

Proper orthogonal decomposition (POD) is a data-driven technique to reduce large-scale, high-dimensional processes or data-sets into low-dimensional deterministic modes (Berkooz et al. 1993; Oberleithner et al. 2015; Taira et al. 2017). POD decomposes snapshots of space and time-dependent observables into orthogonal modes, ranks them according to their energy and obtains the spatial structure of the corresponding modes. Here, we use the snapshot POD method suggested by Sirovich (1987). It has a spatial average operator to extract coherent structures from the time-resolved snapshots of fields such as velocity, pressure, temperature and concentration. The method uses L^2 -norm for classifying the modes, which

is equivalent to the fluctuating kinetic energy for the velocity field and variance for other fields.

The velocity fluctuations (\mathbf{u}') can be decomposed in terms of the spatial modes (Ψ_i) and temporal modes (\mathbf{a}_i) in the following manner:

$$\mathbf{u}'(x, y, t) := \mathbf{u}(x, y, t) - \bar{\mathbf{u}}(x, y) := \sum_{i=1}^N a_i(t) \Psi_i(x, y), \quad (2)$$

where $\bar{\mathbf{u}}(x, y)$ refers to time average of the instantaneous velocity field $\mathbf{u}(x, y, t) = u_x \hat{i} + u_y \hat{j} + u_z \hat{k}$ with a resolution of $m \times n$. Depending upon the component of velocity of interest, we reshape each image as a row and form a two-dimensional matrix that has a size of $N \times (m \times n)$ (Taira et al. 2017), where N is the total number of images. Each snapshot is considered to be an element of the square-integrable vector field $L^2(\xi)$ specified in the Hilbert space. The class of square-integrable functions is unique for compatibility with an inner product, which allows us to define conditions of orthogonality. The inner product of two vector α and β fields in the Hilbert space is defined as

$$(\alpha, \beta)_\xi := \int_\xi \alpha \cdot \beta \, d\mathbf{x}, \quad (3)$$

where, in a spatial domain $\xi \subset \mathbb{R}^3$, \mathbf{x} is a point and the corresponding norm $\|\alpha\|_\xi$ is given by

$$\|\alpha\|_\xi := \sqrt{(\alpha, \alpha)_\xi}. \quad (4)$$

Usually, compared to the number of snapshots, the number of spatial points is significantly bigger. So, we quantify the relation between individual snapshots by formulating the correlation matrix $\mathbf{R}_{(N \times N)}$

$$R_{i,j} := \frac{1}{N} \left[\mathbf{u}'(\mathbf{x}, t_i), \mathbf{u}'(\mathbf{x}, t_j) \right]^T. \quad (5)$$

Here, each snapshot is stored in $\mathbf{x} = x_i$ after reshaping from size ($m \times n$), and T indicates the transpose of the matrix.

Using eigenvalue decomposition, we calculate the eigenvectors and eigenvalues of the correlation matrix \mathbf{R} ,

$$\mathbf{R} \mathbf{a}_i = \lambda_i \mathbf{a}_i. \quad (6)$$

\mathbf{R} has real and non-negative eigenvalues $\lambda_i \geq 0$. We assume the eigenvalues are arranged in decreasing order without losing generality, i.e. $\lambda_1 \geq \lambda_2 \geq \dots \geq \lambda_N$. The eigenvectors \mathbf{a}_i are called the temporal coefficients of the velocity field and follow the orthogonality condition

$$\frac{1}{N} \sum_{k=1}^N a_i(t_k) a_j(t_k) = \lambda_i \delta_{ij}, \quad (7)$$

where δ_{ij} is the Kronecker Delta function.

The spatial modes are determined as follows using the projection of the snapshots on the temporal coefficients,

$$\Psi_i(\mathbf{x}) := \frac{1}{N\lambda_i} \sum_{j=1}^N a_i(t_j) \mathbf{u}'(\mathbf{x}, t_j). \tag{8}$$

The spatial modes are orthogonal by construction, viz. $(\Psi_p, \Psi_q)_\xi = \delta_{pq}$. After reshaping $\Psi_i(\mathbf{x})$, we can get spatial modes $\Psi_i(x, y)$ having m and n as rows and columns, respectively.

Additionally, the correlation between the flow structures and structures in other quantities, such as concentration, temperature, or pressure, can be identified using the POD method. This can be achieved by the extended POD analysis (Borée 2003). The principal objective of employing the extended proper orthogonal decomposition (EPOD) methodology is to provide a common basis for the dominant structures from OH-PLIF and OH*-chemiluminescence fields. This method enables a comparative analysis of the spatial distribution of the dominant structures of the flame surface and the heat release rate distribution fields in correlation with the structures derived from the dominant proper orthogonal decomposition (POD) modes inherent to the flow velocity field. The absence of a common basis precludes the comparison of dominant structures across two or more spatiotemporal datasets, even if acquired simultaneously. The velocity field $u(\mathbf{x}, t)$ is measured concurrently with a collection of intensity fields $I(\mathbf{x}, t)$. $I(\mathbf{x}, t)$ is first decomposed into the average $\bar{I}(\mathbf{x}, t)$ and a fluctuating part $I'(\mathbf{x}, t)$

$$I(\mathbf{x}, t) = \bar{I}(\mathbf{x}, t) + I'(\mathbf{x}, t). \tag{9}$$

Similar to the spatial modes $\Psi(\mathbf{x})$ of velocity, a set of extended POD modes $\Omega_i(\mathbf{x})$ can be defined as

$$\Omega_i(\mathbf{x}) = \frac{1}{N\lambda_i} \sum_{j=1}^N \mathbf{a}_i(t_j) I'(\mathbf{x}, t_j), \tag{10}$$

where $a_i(t_j)$ are the temporal coefficients of the POD modes of velocity fields. In this manner, we correlate coherent structures observed in the swirling flow with the extended modes in the OH-PLIF (I_p) and OH*-chemiluminescence fields (I_C).

3.2 Determination of phase using Hilbert transform

The POD and extended POD analysis quantifies the spatial extent of flow and flame structures. The temporal interactions of these spatially extended modes are equally important, and we quantify these interactions based on their synchronization characteristics. This is achieved by time series analysis of the POD temporal coefficients along with pressure and global heat release rate fluctuations.

We compute the instantaneous phase using the concept of analytic signals and by utilizing the Hilbert transform (Rosenblum et al. 1996). For a given signal $x(t)$, the instantaneous amplitude $A(t)$ and phase $\phi(t)$ can be obtained from the complex analytic signal

$$\xi(t) = x(t) + i\mathcal{H}(x(t)) = A(t) \exp(i\phi(t)) \tag{11}$$

where $A(t)$ and $\phi(t)$ denote the instantaneous amplitude and phase of the analytic signal, respectively. The Hilbert transform is $\mathcal{H}(x(t)) = 1/\pi \int_{-\infty}^{\infty} x(\tau)/(t - \tau) d\tau$, where the integral is evaluated at the Cauchy principal value. The analytic nature of temporal coefficients is verified for different states by plotting the phase space trajectory of $\xi(t)$ and adjudging its centre of rotation. For periodic signals, there is a unique centre of rotation, allowing us to uniquely specify the phase of the signal. As the instantaneous phase is a monotonically increasing or decreasing quantity, it is first wrapped to the interval $[-\pi, \pi]$. Finally, synchronization among pairs of signals is evaluated by measuring the instantaneous phase difference: $\Delta\phi_{x_1, x_2} = \phi_{x_1}(t) - \phi_{x_2}(t)$. Signals are considered to be phase locked when the difference $\Delta\phi_{x_1, x_2}$ becomes bounded to a small interval ϵ ($\leq 2\pi$) around the mean phase C , to wit, $|\Delta\phi_{x_1, x_2}(t) - C| = |\phi_{x_1} - \phi_{x_2} - C| \leq \epsilon$ (Pikovsky et al. 2001).

The temporal interactions of the identified structures are further visualized using phase portraits or Lissajous plots for a pair of signals. The exact relation between the signals is inferred based on the dominant frequencies (f_1, f_2) of the signals and the mean phase difference ($\Delta\phi_m$). This is done by constructing the pair of analytical signals based on the superposition of the dominant frequencies,

$$\begin{aligned} x_1 &= A_1 \sin(2\pi f_1 t + \Delta\phi_m) + A_2 \sin(2\pi f_2 t + \Delta\phi_m), \\ x_2 &= B_1 \sin(2\pi f_1 t) + B_2 \sin(2\pi f_2 t), \end{aligned} \tag{12}$$

where f_1 is the dominating frequency of the signal and f_2 is the multiple of f_1 , i.e. $f_2 = 2f_1$. A_1, A_2, B_1 and B_2 are the amplitudes associated with the dominant modes f_1 and f_2 for different pair of signals. A phase difference between the resultant signals x_1 and x_2 is $\Delta\phi_m$.

3.3 Quantifying chaotic evolution of coherent structures

In order to quantify chaotic time evolution of coherent structures, we perform 0 – 1 test which quantifies the unbounded growth of phase space trajectories typical of chaos (Gottwald and Melbourne 2004). For any input time series $\gamma(t)$, the first step is to compute the translation variables $x(n)$ and $y(n)$ such that

$$x(n) = \sum_{j=1}^n \gamma(t) \cos(tc), \quad y(n) = \sum_{j=1}^n \gamma(t) \sin(tc) \tag{13}$$

where $n = 1, 2, \dots, N$, where N denotes the number of data points present in the time signal. For our analysis, we have selected the value of c in the interval $(\pi/5, 4\pi/5)$ (Nair et al. 2013). The nature of these two translation variables provides indications to determine if chaos exists in the system. For periodic or quasi-periodic oscillations, the variables show bounded behaviour. However, for chaotic dynamics, their behaviour is unbounded and irregular. The evolution of the trajectory in the $x - y$ plane for increasing n can be computed with the help of modified mean square displacement $M(n)$ as follows (Ashwin et al. 2001):

$$M(n) = \frac{1}{N} \sum_{j=1}^n [(x(j+n) - x(j))^2 + (y(j+n) - y(j))^2] - \frac{1}{N} \sum_{j=1}^n \gamma(t) \frac{1 - \cos(jc)}{1 - \cos(c)} \tag{14}$$

For a chaotic state, the displacement $M(n)$ between the translational variables grows monotonically with n , while it becomes nearly constant for regular states. With the use of linear regression, the asymptotic growth rate (K) of the mean displacement is computed as follows:

$$K = \lim_{n \rightarrow \infty} \frac{\log M(n)}{\log n} \tag{15}$$

Gottwald and Melbourne (2009) pointed that for small values of n , the linear regression methods results in altering the value of K . To estimate the value of K , we use a correlation method which performs better than the linear regression method. In this method, K is the correlation coefficients for the vectors $\zeta = (1, 2, 3, \dots, n)^T$ and $\Delta = (M(1), M(2), M(3), \dots, M(n))^T$. Subsequently, the correlation coefficient can be defined as

$$K = \text{corr}(\zeta, \Delta) = \frac{\text{cov}(\zeta, \Delta)}{\sqrt{\text{var}(\zeta)\text{var}(\Delta)}} \in [-1, 1] \tag{16}$$

where

$$\text{cov}(\zeta, \Delta) = \frac{1}{n} \sum_{j=1}^n [\zeta(j) - \bar{\zeta}] [\Delta(j) - \bar{\Delta}],$$

$$\text{var}(\zeta) = \text{cov}(\zeta, \zeta), \quad \text{and} \quad \bar{\zeta} = \frac{1}{n} \sum_{j=1}^n \zeta(j).$$

The value of K lies between 0 and 1. For a chaotic signal, K takes a value close to 1, and for a regular signal, it approaches a value close to 0.

4 Results and discussion

We begin by examining three distinct dynamical states - chaotic, period-1 and period-2 oscillations exhibited by the combustor at different levels of H_2 enrichment. The operating conditions corresponding to these states are highlighted in Table 1. The combustor is initially in a thermoacoustically stable state, operating only on CH_4 at a premixed equivalence ratio of $\phi = 0.65$ and a thermal power of 25.31 kW. During these conditions, thermoacoustic system is characterized with low-amplitude, chaotic pressure oscillations. We refer to this baseline state as chaotic state. When CH_4 -air flame is enriched with H_2 , the pressure fluctuations inside the combustor exhibit high amplitude period-1 and period-2 limit cycle oscillations (LCO) at 50 and 20% hydrogen enrichment. We refer to these states as period-1 and period-2 states, respectively.

We disentangle large-scale coherent structures in the flow velocity field and their impact on the flame surface and heat release rate field by performing the POD and extended POD analysis. Large-scale structures in turbulent flows contain a majority of the turbulent kinetic energy which commences the cascade process and turbulence phenomenology. Thus, POD modes with the largest kinetic energy content along with correlated flame structures would dominate the flow and flame dynamics. This can be observed simply by noting that the turbulent kinetic energy E and fluctuating kinetic energy E_i contained in each POD mode are connected via the relations between the eigenvalues of the correlation matrix (eq. 5) and the flow field fluctuations:

$$E_i := \frac{1}{2} \overline{(\mathbf{u}', \Psi_i)^2} = \frac{1}{2} \lambda_i, \quad E = \sum_{i=1}^N E_i = \frac{1}{2} \sum_{i=1}^N \lambda_i. \tag{17}$$

Figure 2 shows the percentage of the turbulent kinetic energy (E_i/E) that the first 100 modes of the velocity field contain for different dynamical states. For all the cases, the first 100 modes contain over 90% of the turbulent kinetic energy, with the first few principal modes accounting for a major fraction of the total kinetic energy. During chaotic oscillations, the first three POD modes contain 14.74% of the total kinetic energy. Further, for period-1 LCO, the first two modes contain 19.87% of the turbulent kinetic energy. The third mode contains an order of magnitude less fraction of the total energy. The energy content decreases drastically for higher POD modes. For period-2 LCO, the first three modes contain a comparable proportion of the total kinetic energy, with the total amounting to around 29.86% of the total energy.

In keeping with the definition, the spatial structures associated with the first few principal modes are expected to dominate flow field dynamics. For subsequent analysis and

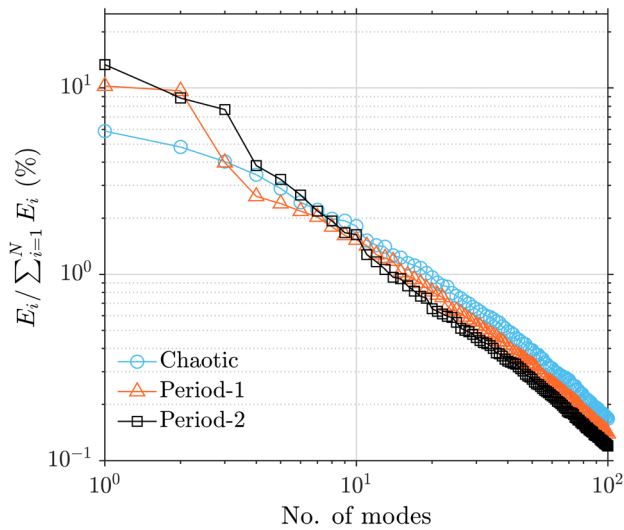


Fig. 2 Fraction of kinetic energy contained in the spectrum of POD modes (eq. 17) obtained from the flow velocity field (\mathbf{u}') for the three dynamical states highlighted in Table 1. The key role played by large-scale coherent structures during the states of thermoacoustic instabilities (period-1 and period-2) is highlighted by the first two principal modes containing an order of magnitude higher kinetic energy than observed during stable operation

visualization, we consider the transverse component of the velocity field (u_x) and its effect on the turbulent flame. Our conclusions remain the same when the axial component (u_y) is considered instead (see supplementary information).

4.1 Chaotic oscillations in the absence of H_2

The flow and flame dynamics of the swirl combustor operating only on CH_4 at $\phi = 0.65$ are shown in Fig. 3. The first row shows the mean of the transverse velocity component (\bar{u}_x), the flame brush obtained from time-averaged OH-PLIF imaging (\bar{I}_p) and the mean heat release rate obtained from OH*-chemiluminescence imaging (\bar{I}_C). The time averaging is performed over 3000 instantaneous images (or 0.3 s). Figure 3a shows high transverse velocity along the shear layers, with the opposite signs indicating the clockwise direction of the swirling flow. In addition, the flow shows very weak inner and outer recirculation (also shown from Fig. 2a showing \bar{u}_y , in supplementary materials). Hence, the flame can be seen to stabilize along the inner shear layer, resulting in a characteristic V-shape of the turbulent flame brush (Fig. 3b). The thickness of the flame brush can also be seen to increase downstream in comparison with the attachment point at the exit of the dump plane. As chemiluminescence images are line-of-sight integrated in the out-of-plane direction, increased flame brush thickness can be seen to result in a sustained, continuous band of heat release rate profile downstream of the combustor (Fig. 3c).

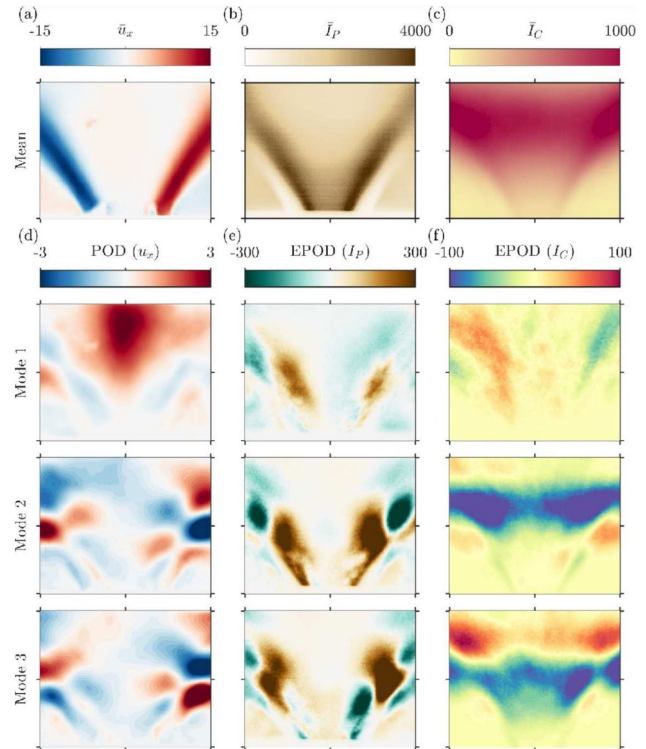


Fig. 3 Flow and flame dynamics for the purely CH_4 -air flame for the baseline condition. Mean of the (a) transverse velocity component u_x , (b) flame brush obtained from OH-PLIF images, and (c) heat release rate fluctuations obtained from OH*-chemiluminescence. Panels (d–f) show the first three POD modes of u'_x and the extended modes associated with I'_p and I'_C

Figure 3d shows the first three POD modes of the transverse (u_x) velocity, together which account for 14.74% of TKE energy (Fig. 2). The first POD mode of the transverse velocity shows a coherent structure that grows in magnitude in the streamwise direction. The structure indicates a vortex bubble with positive velocity magnitude, depicting the overall direction of its motion. In contrast, mode 2 and mode 3 depict modes with the same wavenumber and frequency, whose magnitude increases and then decays downstream. These structures are shifted in the streamwise direction by approximately a quarter wavelength. Mode 2 and 3 are part of an oscillating process, linked to a helical mode instability around the recirculation bubble observed in POD mode 1. This can be observed in the Lissajous plot between mode coefficients $a_2 - a_3$ (Fig. 4). We further note here that the first three POD modes associated with u_y along the shear layer (in Fig. 2d in supplemental materials) also indicate the presence of the same coherent structures with the same axial wavenumber with each mode shifted axially. Additionally, all three modes exhibit an advection of the central recirculation zone (in Fig. 2d in supplemental materials).

The extended POD modes of the flame profile (I_p) associated with the POD modes of u_x are also shown in Fig. 3e.

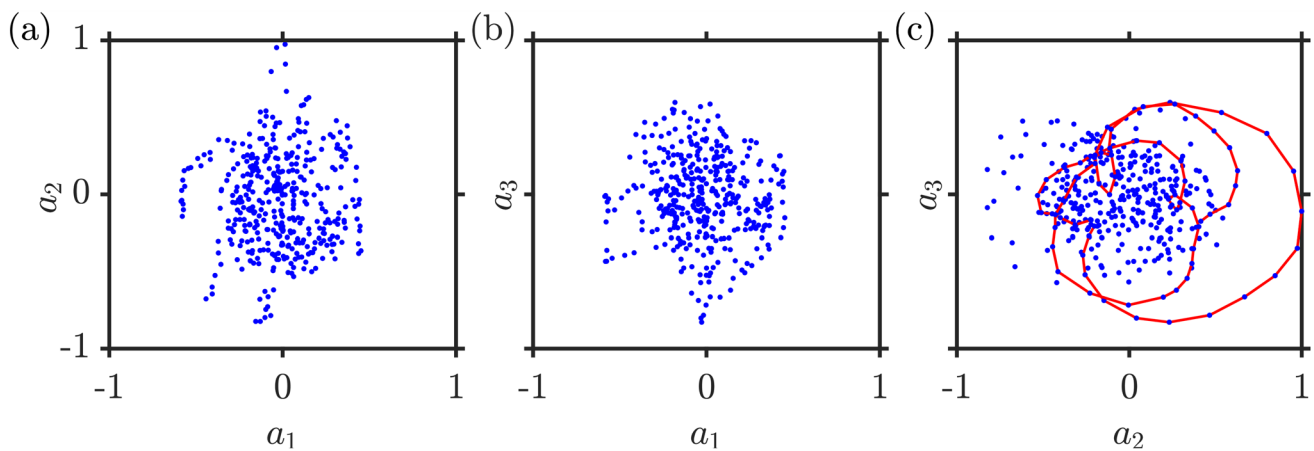


Fig. 4 (a–c) Phase portrait of the pairs of temporal coefficients ($a_1 - a_3$) of the velocity field for the state of chaotic oscillations. The red lines in (c) indicate a few periodic orbits

We notice a number of salient features of the flame dynamics from the extended POD modes of the flame surface I_p in Fig. 3e. The dominant POD mode of u_x associated with the central recirculation bubble does not correlate with extended POD modes of the flame surface. Only the weaker structures along the shear layer are reflected in the extended POD modes of the flame surface. This is due to the V-shaped flame (Fig. 3b) which stabilizes along the inner shear layer and does not extend into the inner recirculation zone. The increased activity in the flame surface is further emphasized in the second and third extended POD modes of the flame surface. The coherent structures present along the shear layer in the second and third POD modes of u_y are clearly correlated with the extended POD mode structures. The extended POD mode structure is also shifted by a quarter wavelength. The amplitude of the structure can be seen to increase downstream of the flame attachment region, identifying regions contributing to most of the changes in the flame dynamic. Interestingly, while the coherent structure is anti-symmetric (mode 2 & 3 in Fig. 3d) due to helicoidal instability in the flow field, the extended mode structure of the flame surface clearly retains axisymmetry.

The effect of these local flow and flame dynamics on the global heat release rate profile can be understood from the extended mode structure of heat release rate distribution shown in Fig. 3f. As with the extended structure of the flame surface, the first extended mode of heat release rate does not correlate with the central recirculating zone, corroborating the fact that the central vortex bubble arising due to the swirl does not affect the fluctuations in the heat release rate. The second and third extended modes, on the other hand, correlate well with the coherent structure present in the velocity field. Indeed, we notice that the structure of extended POD of heat release exists along the shear layers along with the extended mode structure of the flame surface. The second

and third modes are again related to the same structure, only displaced by a quarter wavelength. The banded nature of these structures can be ascribed to the fact that the chemiluminescence imaging is line-of-sight integrated, revealing the annular region over which heat is released from the three-dimensional flame structure. We note here that our observations remain the same when the streamwise velocity u_y is used for obtaining extended POD modes from the flame surface and heat release rate (see Fig. 2e,f in supplemental materials). These observations show that the structures from the heat release rate distribution and flame surface corresponding to the most dominant POD mode do not correlate. The coherent structures from other modes show some correlation with the structures from other fields. However, due to the low turbulent kinetic energy of modes 2 and 3, their overall effect remains minimal.

We next relate the manner in which these spatial modes are related to the thermoacoustic response in the system. Figure 5 presents the normalized time series of the acoustic pressure (p') and heat release rate fluctuations (\dot{q}') along with the time evolution of the temporal coefficients of the first three POD modes. Here, $\dot{q}'(t)$ is obtained by a global summation from individual chemiluminescence images. Each of the time series is normalized by their respective maxima to aid comparison. The aim is to relate the manner in which the spatial modes evolve in time and relate to fluctuations in p' and \dot{q}' . In each case, the time evolution is characterized by the power spectral density and the phase portrait of the analytic signal defined according to (eq. 11).

The present baseline case corresponds to the low-amplitude stable operation of the combustor. The pressure and heat release rate oscillations during this baseline case remain chaotic, as reported earlier in (Kushwaha et al. 2021). This can be observed in Fig. 5b where the power spectral density for p' , \dot{q}' and the temporal coefficients

Fig. 5 Characterization of the thermoacoustic response during the state of chaotic oscillations. (a) Time series and (b) power spectra of fluctuations in acoustic pressure, heat release rate and the temporal coefficients of the first three POD modes. (c) Phase space trajectory in the complex analytical plane for the part of the signals indicated in panel (a)

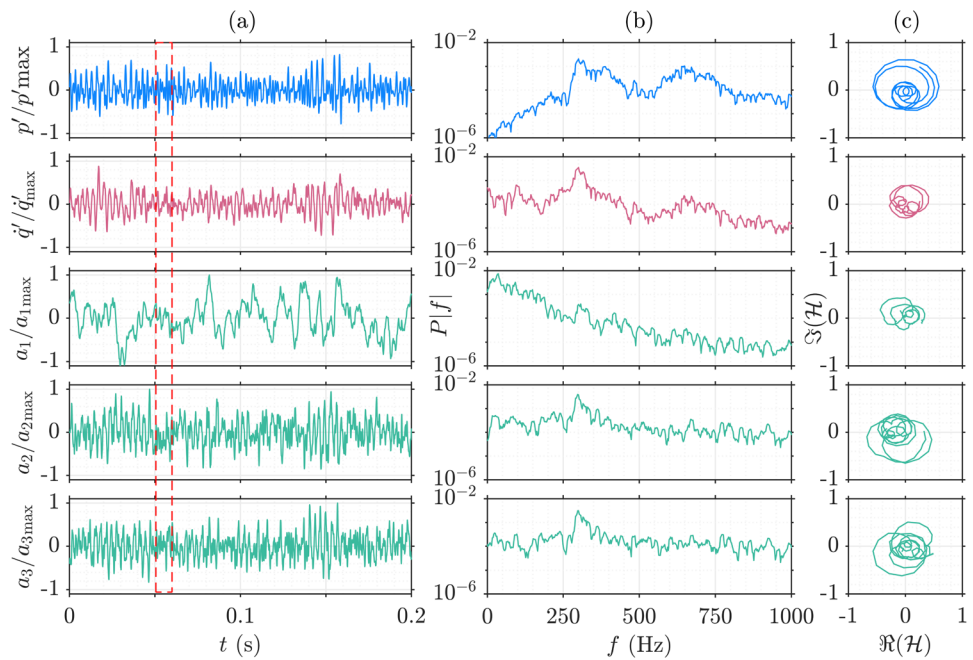


Table 2 Results of the 0-1 test for different signals during all the dynamical states discussed in this paper

Dynamical states → Signals ↓	Chaotic oscillations	Period-1 LCO	Period-2 LCO
p'	0.99	0.08	0.01
\dot{q}'	0.98	0.11	0.05
a_1	0.62	0.15	0.27
a_2	0.99	0.12	0.32
a_3	0.99	0.61	0.79

The values close to 1 indicate the existence of chaos in the signal. Moreover, the signal with regular dynamics show values close to 0

(a_1, a_2, a_3) depict a broadband behaviour. In addition, the phase portrait featuring the analytic representation of these signals depicts the absence of a unique centre of rotation. Hence, the signals are non-analytic, and a phase cannot be ascribed to these signals.

We perform the 0-1 test (described in Sect. 3.3) for these signals to ascertain whether their dynamics is chaotic or not. The value of the asymptotic growth rate K of the displacement M between translational variables is tabulated in Table 2. We note here that all the signals display values which are close to unity, implying the chaotic evolution of each of these quantities. Thus, the heat release rate and pressure oscillations display chaos during stable combustor operation, corroborating past results (Nair and Sujith 2014; Kushwaha et al. 2021).

4.2 Period-1 limit cycle oscillations at 50% H₂ enrichment

The combustor shows the state of TAI with the addition of hydrogen (50%) at a constant equivalence ratio of $\phi = 0.65$ and a thermal power of $P = 20$ kW. We observe sustained, period-1 LCO with an amplitude of $p'_{rms} = 0.91$ kPa. Figure 6 shows the time-averaged velocity field, flame brush and heat released rate. Figure 6a shows high transverse velocity along the shear layers having opposite signs which indicate swirling flow. The shear layer is much broader in comparison with the baseline case. The flame also stabilizes along the shear layers and extends towards the outer recirculation zone, making it an M-shaped flame (Fig. 6b). The flame can be seen to be anchored very close to the dump plane. The time-averaged image of the heat release distribution field shows a concentrated region of high heat release rate. The location of the peak of \bar{I}_C is located much closer to the flame anchor point, in contrast to the baseline chaotic case where the peak occurred much further downstream.

Figure 6d shows the first three dominant POD modes associated with the transverse velocity fluctuations u'_x . These three modes collectively hold 30% of the total kinetic energy. The first and second POD modes indicate the presence of the same coherent structure in the form of a toroidal vortex of the same frequency and wavenumber. The modes can be seen to be shifted by a quarter of a wavelength and $\pi/2$ radians (see Fig. 9a). In contrast to the baseline case, the dominant coherent structure during period-1 LCO comprises the helical toroidal vortex. The amplitude of the toroidal vortex can be observed to be much stronger than it was for

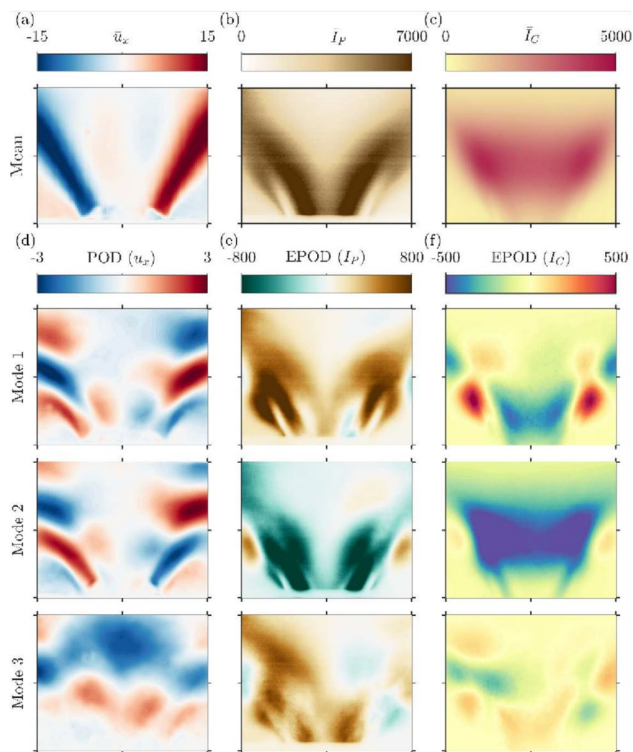


Fig. 6 Flow and flame dynamics during Period-1 TAI with 50% hydrogen enrichment. Mean of the (a) transverse velocity component \bar{u}_x , (b) flame brush obtained from OH-PLIF images, and (c) heat release rate fluctuations obtained from OH*-chemiluminescence. Panels (d–f) show the first three POD modes of u'_x and the extended modes associated with I'_p and I'_C

the baseline case (cf. Fig. 3). The toroidal vortex can also be seen to extend to a much larger radial domain, with the anti-phase features alternating asymmetrically on each side of centre flow axis ($x = 0$). In addition to the toroidal vortex, the first two POD modes also show the presence of an anti-symmetric mode structure along the IRZ which convects in time. The third mode shows the presence of an axisymmetric coherent structure extending along the length of the combustor.

The extended POD modes of the flame surface are shown in Fig. 6e. For the first two modes, we notice that the extended structure is distinctly M-shaped with branches of the flame surface extending along the nodal line of the toroidal as well as the inner coherent structure. The two extended modes, which are shifted by $\pi/2$ radians, are associated with positive and negative intensities, indicating the correlation between the POD mode and the extended POD mode structure of the flame surface. In addition, the first and the second EPOD modes have the maximum intensity along the shear layers. However, we observe small-scale structures in the third EPOD mode structure of the flame. Figure 6f presents the EPOD modes of the heat release rate distribution. The first two EPOD modes show the structures in the IRZ and

along the shear layer. The structures along the shear layer confirm the existence of a toroidal vortex in the flow field (Fig. 8d). However, we do not observe the high-intensity structure in the third EPOD modes of the OH-PLIF images and OH*-chemiluminescence. With the random arrangement of structures in the third extended mode of the flame surface and heat release rate, the coherent structures from the flow field do not correlate with the inner recirculating zone.

To probe the dynamics further, the time series, power spectra and analytical signal are shown in Fig. 7. The time series of p' and q' signals, normalized with their respective global maxima values, show high amplitude fluctuations compared to that during the chaotic oscillations (Fig. 7a). We also observe a distinct peak at 415 Hz and its higher harmonic at 827 Hz for the p' and q' signals (Fig. 7b). The temporal coefficients a_1 and a_2 are periodic in nature (Fig. 7a) and exhibit distinct peak at 415 Hz (Fig. 7b). However, the third mode does not show periodic behaviour (Fig. 7a) and we observe a broadband power spectrum without any distinct peak (Fig. 7b). However, the temporal coefficient of the third mode shows aperiodic behaviour (Fig. 7a) and exhibits a broadband power spectrum without any distinct frequency peak (Fig. 7b). The trajectory on the complex plane also does not have a unique centre of rotation, indicating that the signal is not analytic. Further, from Table 2, we notice that the $0 - 1$ test of a_1 indicates a value of $K = 0.61$, indicating a possible chaotic evolution of mode 3.

In order to understand the coupled behaviour between the variables, we show the Lissajous plots and determine the phase difference between various pairs of signals in Fig. 8. The phase space trajectory plotted in the complex analytic plane, shown in Fig. 7c, clearly depicts a unique centre of rotation for all the pair of signals except for a_3 . This indicates that all signals other than a_3 are analytic in nature and their phases are well-defined. We compute the mean of the instantaneous phase difference and show it with a red line. With the help of dominant frequencies and the mean phase difference for each pair of signals, we generate the analytical curve according to (12) and depict it in the Lissajous plot. These analytical curves identify the phase and frequency relationship among the dominant POD modes and the pressure and heat release rate fluctuations. We further note that the pressure fluctuations correspond to the acoustic standing wave of the combustor, ensuring that the phase jumps by 2π when the nodal line is crossed. Thus, the phase relationships discussed next are expected to remain unchanged close to the dump plane of the combustor where the POD are shown in Fig. 7.

In Fig. 8a, the phase plot between a_1 and a_2 shows that the first two POD modes are phase-locked around $\pi/2$ and are part of the same oscillating coherent structure. We also notice that p' and q' are phase-locked close to a mean value of $\langle \Delta\phi \rangle = \pi/3$ (Fig. 8d), implying that the Rayleigh criteria

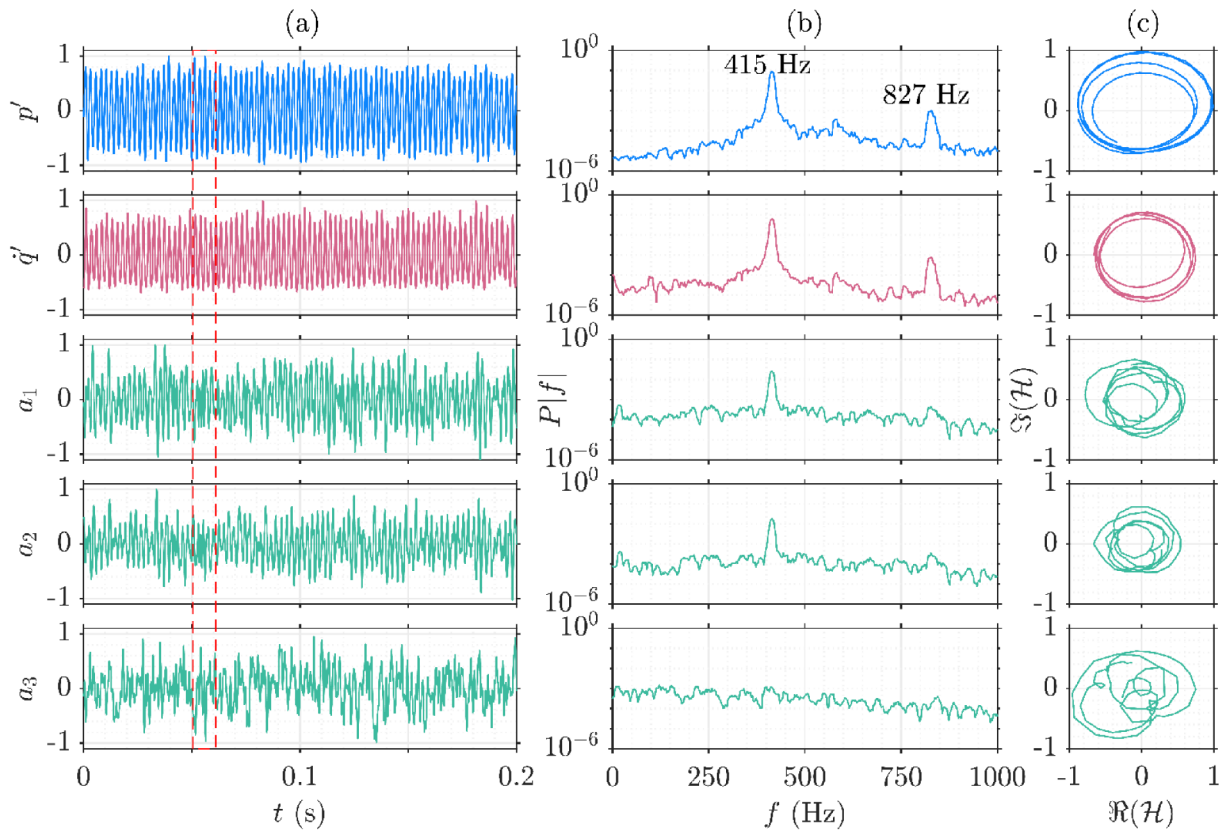


Fig. 7 Characterization of the dynamic response during period-1 TAI. **(a)** Time series and **(b)** power spectra of acoustic pressure, heat release rate and temporal coefficients of the first three POD modes.

The time series are normalized by their respective maxima values. **(c)** Phase space trajectory in the complex analytical plane for the part of the signal indicated in panel **(a)**

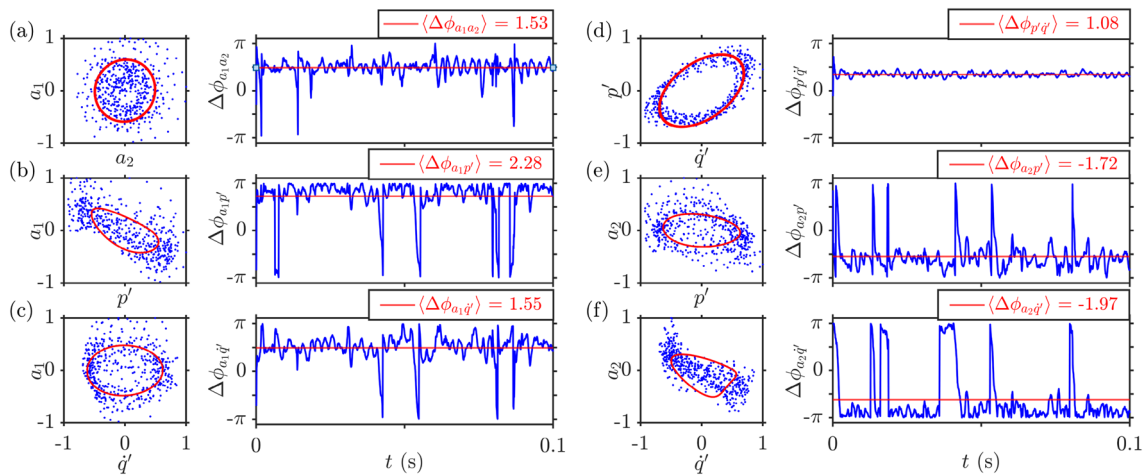


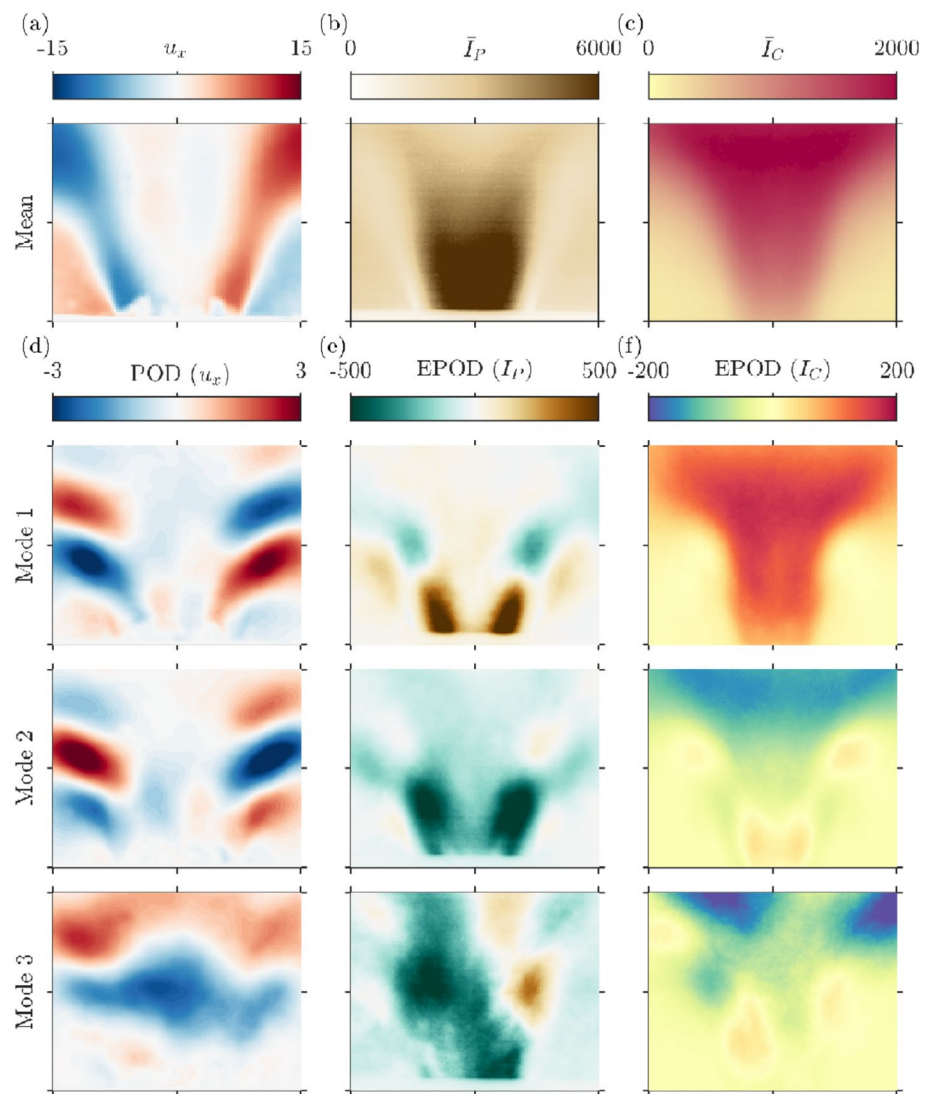
Fig. 8 (a–f) Phase portrait of the temporal coefficients of the flow velocity field with respect to acoustic pressure and heat release rate along with analytical curves having the same dominating frequen-

cies and phase differences as the original data and the corresponding phase difference with the red line indicating the mean value of phase difference, for the state of TAI with period-1 LCO

are fulfilled during the state of TAI. $\langle \cdot \rangle$ indicates a time-averaged value. The relationships between the dominant POD modes and p' and q' are quite interesting. We note that a_1 is

phase-locked to p' at $\Delta\phi = 3\pi/4$ denoted by the elliptical Lissajous plot (Fig. 8b) and to q' at $\Delta\phi = \pi/2$ as denoted by the circular plot (Fig. 8c). Next, we notice that the second

Fig. 9 Mean of the (a) transverse velocity component u_x , (b) flame brush obtained from OH-PLIF images, and (c) heat release rate fluctuations obtained from OH*-chemiluminescence. Panels (d–f) show the first three POD modes of u_x and the extended modes associated with I_p' and I_C' for the state of period-2 LCO with 20% hydrogen by volume of the fuel



mode a_2 , which is associated with the same dominant coherent structure, is phase-locked to p' at $-\pi/2$ (Fig. 8e) and with \dot{q}' with a phase difference of $\approx -5\pi/8$.

One of the mechanisms through which the state of TAI occurs is often related to the presence of coherent structures. Previous researches have shown that the heat release rate fluctuations induced by the coherent structures are in-phase with the pressure fluctuations (Poinsot et al. 1987; Chakravarthy et al. 2007; Pawar et al. 2017). However, the phase relationships presented above suggest a non-trivial manner in which the coherent modes interact with p' and \dot{q}' fluctuations. The present relationship suggests that most energetic coherent structures evince heat release rate fluctuations delayed by a phase-lag of $\pi/2$, which are subsequently related to p' fluctuations after a phase delay of $\pi/3$. However, the mismatch between the mean-phase relationship obtained from $\langle \Delta\phi_{a_1, p'} \rangle$ and $\langle \Delta\phi_{a_1, \dot{q}'} \rangle$ with $\langle \Delta\phi_{p', \dot{q}'} \rangle$ indicates

additional mechanism through which the coherent structure is coupled to the pressure fluctuations.

Thus, we have identified the phase relationships between the coherent structures containing most of the energy, flame fluctuations, global heat release rate fluctuations and the pressure field. The structures from the flame surface at the central plane and heat release rate distribution field are highly correlated with the coherent structures from the velocity field and temporally show the 1:1 frequency locking behaviour among the subsystems in the combustor.

4.3 Period-2 limit cycle oscillations (P2 LCO)

Let us now turn our attention to the coupled dynamics observed during the state of TAI with period-2 LCO when the combustor is operated at a constant equivalence ratio $\phi = 0.65$ and thermal power $P = 20$ kW with only 20% hydrogen. Like earlier, we plot the mean, POD modes and

extended POD modes in Fig. 9 and the temporal dynamics in Fig. 10.

In the mean transverse velocity field (Fig. 9a), we notice high-velocity fluctuations along the shear layers and the outer recirculation region (ORZ) with the opposite signs. The strength of fluctuations is lower than that observed during period-1 LCO (Fig. 6a). Moreover, the mean of the OH-PLIF image shows the presence of a columnar-shaped flame having very high intensity stabilized along the inner recirculation zone of the combustor (Fig. 9b). Most of the heat release rate occurs along the inner recirculation zone and extends downstream of the combustor as shown in Fig. 9c. This is in contrast to the mean profile observed for the M-flame during period-1 oscillations (Fig. 6a). These results indicate that the flame surface shape and the heat release rate distribution are entirely changed from the state of period-1 LCO with a small variation in the volume of hydrogen to the fuel.

To study the state of period-2 LCO thoroughly, the first three dominating POD modes of the transverse component are presented in Fig. 9d which cumulatively contains 23% of the total kinetic energy. The first two modes show that the coherent structures are symmetrically positioned on each side of the flow axis and have anti-phase behaviour. These coherent structures confirm the existence of the helical nature of the flow. Moreover, very weak small-scale coherent structures with low-velocity fluctuations can also be seen in IRZ. Unlike during period-1 LCO (Fig. 6d), the coherent structure can be seen to be limited only along the periphery and do not extend inwards along the shear layer. However, the third mode shows the presence of a convecting structure along the axial direction (Fig. 9d). We also see similar elongated coherent structures in the POD modes of the axial velocity component (see Fig. 4 in supplementary material). These observations show that the flow structures from the dominant modes confirm the existence of helical instability. However, the heat release rate field indicates that the maximum heat release occurs in the IRZ and does not follow the path of the helical structures in the flow.

The EPOD modes of the flame surface corresponding to the first and second POD modes of velocity field exhibit structures with high flame surface fluctuations along the shear layer near to the inlet of the combustor (Fig. 9e). A longer flame in comparison with that in period-1 LCO appears due to a low volume of hydrogen in the methane. The combustion with a high volume of hydrogen in the fuel has a smaller flame (Zhen et al. 2012). The EPOD modes of the flame surface correlate well with the convecting coherent structure. Moreover, the third EPOD mode shows an asymmetrically distributed flame surface, convecting downstream with the flow (Fig. 9e). We also see similar structures near the IRZ in the extended modes of the flame surface using the axial velocity component of the flow (figure 4 in

Supplementary material). The first two EPOD modes of heat release rate distribution confirm that the maximum heat release rate occurs downstream of the combustor (Fig. 9f). The first two EPOD modes of heat release rate distribution are symmetrical about the axis at $x = 0$. Similar to the third EPOD mode of the OH-PLIF images, the structures occur without any pattern in the third EPOD mode of the heat release rate distribution field. The results from the first two modes clarify that the spatial locations of the coherent structures do not match with the locations of structures from EPOD modes. The coherent structures in the POD modes of axial velocity component share the spatial positions with the structures from the corresponding EPOD of flame surface and heat release rate distribution fields (Fig. 4 in Supplementary material). Moreover, the structures from EPOD modes of flame surface and heat release rate distribution fields match.

To understand the time dynamics of the state of period-2 LCO, we show the time series, power spectra and analytical signal in Fig. 10. The normalized time series of p' and \dot{q}' signals show high amplitude fluctuations. The acoustic pressure shows period-2 LCO, characterized by two dominant timescales. We observe that the signal repeats itself in every two oscillations. The heat release rate signal shows period-1 LCO (Fig. 10a) that is shown in our previous study (Kushwaha et al. 2021). The power spectra of p' and \dot{q}' show a distinct peak at 283 Hz with its higher harmonics at 566 Hz and 849 Hz. The fundamental frequency and first harmonic in the p' power spectrum have the same order of power (Fig. 10b). On the complex plane, the trajectory of the analytical signal forms a double-looped pattern. We observe a unique centre of rotation for the trajectory for \dot{q}' (Fig. 10c) indicating that the signals are analytic. The temporal coefficients a_1 and a_2 have period-2 behaviour (Fig. 10a) and exhibit distinct peaks at 283 Hz with higher harmonics at 566 Hz and 849 Hz (Fig. 10b). The signals a_1 and a_2 , exhibiting the centres of rotation on the complex plane, are analytic (Fig. 10c). In the case of the third mode, we do not see a periodic behaviour in the time series, as can be seen in Fig. 10a. Further, we notice a broadband spectrum without any distinct peak in the power spectrum (Fig. 10b). The trajectory of the signal does not have a unique centre of rotation (Fig. 10c) which suggests that the signal is not analytic.

In Fig. 11, we show the phase portraits for different pairs of signals and the phase difference between the signals for the corresponding pairs for the state of TAI with period-2 LCO. Unlike the state of period-1 LCO, we observe different patterns similar to the Lissajous figures. The phase portrait for the pair of the signals a_1 and a_2 shows that the coherent structures are phase-locked with the phase difference around $\pi/2$ (Fig. 11a). The reconstructed curve exhibits the circular pattern which confirms the 1:1 frequency locking between a_1 and a_2 . The pair of the signals a_1 and p' show

Fig. 10 (a) time series of acoustic pressure, heat release rate and temporal coefficients of first three POD modes normalized by their respective maxima values; (b) the corresponding power spectra and (c) the analytical signals in the complex plane, corresponding to the time series enclosed in the red dashed box during the state of period-2 LCO

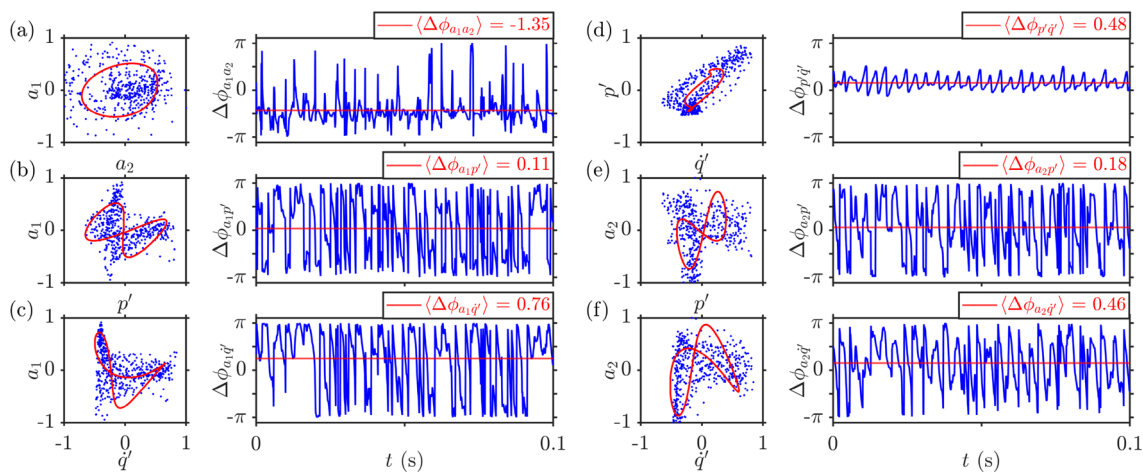
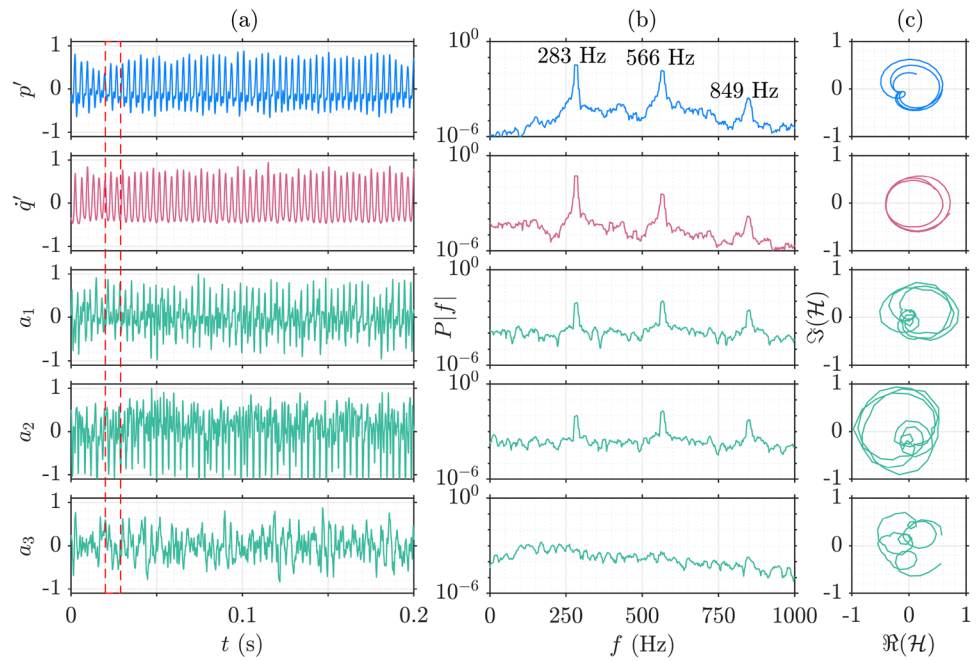


Fig. 11 (a–f) Phase portrait of the temporal coefficients of the flow velocity field with respect to acoustic pressure and heat release rate along with analytical curves having the same dominating frequencies

and phase differences as the original data and (i–vi) the corresponding phase difference with the red line indicating the mean value of phase difference, for the state of TAI with P2 LCO

the phase locking behaviour with the mean phase difference between 0 and $\pi/4$ (Fig. 11a). However, the instantaneous phase difference between a_1 and p' varies a lot which could be due to the presence of high turbulence in the flow. The reconstructed curve in the phase portrait shows a double-lobbed pattern (Fig. 11a) which is the same as the Lissajous patterns, indicating 2:1 frequency locking behaviour. Similarly, other pairs of signals also exhibit the patterns with the two lobes (Fig. 11c–f), which are traditionally observed for 2:1 frequency locking between the signals. The traditional 2:1 Lissajous patterns have lobes with equal shape and size

(at least symmetric about one axis). However, we observe patterns with unequal shape and size due to the presence of higher harmonics in the experimental data. These results confirm that the temporal dynamics have both 1:1 and 2:1 frequency-locking behaviour during the state of TAI with period-2 LCO.

Consequently, we have found that there is a phase relationship among the dominant coherent structures of the flow velocity field, the acoustic pressure field and the heat release rate field. The flame surface structures are highly correlated with the structures in heat release rate. However,

these structures contribute less to the coherent structures of the flow velocity field. Temporal analysis reveals that the subsystems of the combustor demonstrate the 1:1 and 2:1 frequency locking behaviour.

5 Conclusion

In this paper, we apply a framework for analysing the synchronization characteristics of multiple flow parameters that are acquired simultaneously. This framework utilizes the extended proper orthogonal decomposition to look for correlations between coherent structures observed in planar velocity field measurements and parameters such as heat release rate, acoustic pressure fluctuations and OH-distribution. We characterize the coherent structures in the flow field using the proper orthogonal decomposition (POD) technique. We also describe the structures in the OH-PLIF images and heat release rate distribution field using extended POD during the occurrence of various dynamical states of chaotic oscillations and thermoacoustic instability with period-1 and period-2 limit cycle oscillations. These dynamical states are observed with the variation of the amount of hydrogen in the fuel by keeping the thermal power and equivalence ratio constant.

During the state of chaotic oscillations, we hardly find correlations among the structures in the flow, the flame and heat release rate distribution fields. Moreover, the second and third EPOD modes of the flame surface and the heat release rate distribution exhibit increased activity in the flame structures and heat release rate. However, during the state of P1 LCO, we observe that the structures with high energy coherent structures correlate with the high energy structures of the flame surface and heat release rate distribution fields as the structures occur at the same spatial regions. Furthermore, this overlapping of structures decreases from the third mode. During the P2 LCO, the structures from the flame surface are strongly correlated with the structures of the heat release rate field. However, the structures from these fields contribute less to the coherent structures of the velocity field. The spatial overlapping of the structures from different spatial fields plays an important role in correlation among these structures.

The time series analysis shows that the temporal coefficients of the first two modes dominate and decide the nature of the flow field during thermoacoustic instability with period-1 and period-2 limit cycle oscillations. Moreover, the patterns in the phase portrait of different pairs of signals demonstrate 1:1 frequency locking behaviour among the acoustic field, heat release rate and the flow field during period-1 limit cycle oscillations. In the case of period-2 limit cycle oscillations, we see both 1:1 and 2:1 frequency locking behaviour.

Thus, with the help of temporal coefficients of dominating POD modes of the flow field, we apply a framework to understand the synchronization of the flow velocity field with the acoustic pressure and the unsteady heat release rate. Apart from this, we also find the correlations of the coherent structures in a flow field with the flame and the unsteady heat release rate distribution field using the EPOD modes of OH-PLIF images and OH*-chemiluminescence fields. This study enhances the fundamental understanding of how coherence in the flow velocity and heat release rate distributions leads to different types of thermoacoustic instabilities which can occur in practical gas turbines.

Supplementary Information The online version contains supplementary material available at <https://doi.org/10.1007/s00348-024-03845-6>.

Acknowledgements Abhishek Kushwaha would like to acknowledge the Ministry of Human Resource Development, India, for providing Ph.D. scholarship. The authors would like to acknowledge Dr. Samadhan A. Pawar (UTIAS, Canada) for helpful discussions on this topic.

Funding This project has received funding from the European Research Council (ERC) under the European Union's Horizon 2020 research and innovation program (Grant Agreement No. 682383). This research work was also supported by the IoE initiative (SB/2021/0845/AE/MHRD/002696), IIT Madras, India.

Declarations

Conflict of interest The authors report no conflict of interest.

References

- Æsøy E, Aguilar JG, Wiseman S et al (2020) Scaling and prediction of transfer functions in lean premixed H₂/CH₄-flames. *Combust Flame* 215:269–282
- Ashwin P, Melbourne I, Nicol M (2001) Hypermeander of spirals: local bifurcations and statistical properties. *Physica D* 156(3–4):364–382
- Berkooz G, Holmes P, Lumley JL (1993) The proper orthogonal decomposition in the analysis of turbulent flows. *Annu Rev Fluid Mech* 25(1):539–575
- Birol F (2019) The future of hydrogen: Seizing today's opportunities. Report prepared by the IEA for the G20, 82–83, Japan
- Borée J (2003) Extended proper orthogonal decomposition: a tool to analyse correlated events in turbulent flows. *Exp Fluids* 35(2):188–192. <https://doi.org/10.1007/s00348-003-0656-3>
- Boxx I, Stöhr M, Carter C et al (2010) Temporally resolved planar measurements of transient phenomena in a partially pre-mixed swirl flame in a gas turbine model combustor. *Combust Flame* 157(8):1510–1525
- Candel S, Durox D, Ducruix S et al (2009) Flame dynamics and combustion noise: progress and challenges. *Int J Aeroacoust* 8(1):1–56
- Candel S, Durox D, Schuller T et al (2014) Dynamics of swirling flames. *Annu Rev Fluid Mech* 46:147–173. <https://doi.org/10.1146/annurev-fluid-010313-141300>
- Chakravarthy S, Sivakumar R, Shreenivasan O (2007) Vortex-acoustic lock-on in bluff-body and backward-facing step combustors. *Sadhana* 32(1):145–154. <https://doi.org/10.1007/s12046-007-0013-y>

- Choi J, Rusak Z, Kapila A (2007) Numerical simulation of premixed chemical reactions with swirl. *Combust Theor Model* 11(6):863–887. <https://doi.org/10.1080/13647830701256085>
- Chtereov I, Boxx I (2019) Flame topology and combustion instability limits of lean premixed hydrogen enriched flames. In: 27th International Colloquium on the Dynamics of Explosions and Reactive Systems, Jul 28 - August 2, Beijing, China, DOI: <https://elib.dlr.de/130096/>
- Chtereov I, Boxx I (2021) Effect of hydrogen enrichment on the dynamics of a lean technically premixed elevated pressure flame. *Combust Flame* 225:149–159. <https://doi.org/10.1016/j.combustflame.2020.10.033>
- Chu BT (1965) On the energy transfer to small disturbances in fluid flow (part i). *Acta Mech* 1(3):215–234. <https://doi.org/10.1007/BF01387235>
- Cozzi F, Coghe A (2006) Behavior of hydrogen-enriched non-premixed swirled natural gas flames. *Int J Hydrog Energy* 31(6):669–677. <https://doi.org/10.1016/j.ijhydene.2005.05.013>
- Davis D, Therkelsen P, Littlejohn D et al (2013) Effects of hydrogen on the thermo-acoustics coupling mechanisms of low-swirl injector flames in a model gas turbine combustor. *Proc Combust Inst* 34(2):3135–3143. <https://doi.org/10.1016/j.proci.2012.05.050>
- Dowling AP (1997) Nonlinear self-excited oscillations of a ducted flame. *J Fluid Mech* 346:271–290. <https://doi.org/10.1017/S0022112097006484>
- Duwig C, Iudiciani P (2010) Extended proper orthogonal decomposition for analysis of unsteady flames. *Flow, Turbu Combust* 84(1):25–47. <https://doi.org/10.1007/s10494-009-9210-6>
- Emadi M, Karkow D, Salameh T et al (2012) Flame structure changes resulting from hydrogen-enrichment and pressurization for low-swirl premixed methane-air flames. *Int J Hydrog Energy* 37(13):10397–10404. <https://doi.org/10.1016/j.ijhydene.2012.04.017>
- Figura L, Lee JG, Quay BD, et al (2007) The effects of fuel composition on flame structure and combustion dynamics in a lean premixed combustor. In: Turbo Expo: power for Land, Sea, and Air, pp 181–187. <https://doi.org/10.1115/GT2007-27298>
- Freitag M, Janicka J (2007) Investigation of a strongly swirled unconfined premixed flame using LES. *Proc Combust Inst* 31(1):1477–1485. <https://doi.org/10.1016/j.proci.2006.07.225>
- Gallaire F, Ruith M, Meiburg E et al (2006) Spiral vortex breakdown as a global mode. *J Fluid Mech* 549:71–80. <https://doi.org/10.1017/S0022112005007834>
- García-Armingol T, Hardalupas Y, Taylor A et al (2014) Effect of local flame properties on chemiluminescence-based stoichiometry measurement. *Exp Therm Fluid Sci* 53:93–103. <https://doi.org/10.1016/j.expthermflusci.2013.11.009>
- George NB, Unni VR, Raghunathan M et al (2018) Pattern formation during transition from combustion noise to thermoacoustic instability via intermittency. *J Fluid Mech* 849:615–644. <https://doi.org/10.1017/jfm.2018.427>
- Gottwald GA, Melbourne I (2004) A new test for chaos in deterministic systems. *Proc R Soc London, Ser A: Math Phys Eng Sci* 460(2042):603–611. <https://doi.org/10.1098/rspa.2003.1183>
- Gottwald GA, Melbourne I (2009) On the implementation of the 0–1 test for chaos. *SIAM J Appl Dyn Syst* 8(1):129–145
- Greenslade TB Jr (1993) All about Lissajous figures. *Phys Teach* 31(6):364–370
- Guo H, Tayebi B, Galizzi C et al (2010) Burning rates and surface characteristics of hydrogen-enriched turbulent lean premixed methane-air flames. *Int J Hydrog Energy* 35(20):11342–11348. <https://doi.org/10.1016/j.ijhydene.2010.07.066>
- Guo S, Wang J, Zhang W et al (2020) Effect of hydrogen enrichment on swirl/bluff-body lean premixed flame stabilization. *Int J Hydrog Energy* 45(18):10906–10919. <https://doi.org/10.1016/j.ijhydene.2020.02.020>
- Gupta AK, Lilley DG, Syred N (1984) Swirl flows. Tunbridge Wells
- Halter F, Chauveau C, Gökalp I (2007) Characterization of the effects of hydrogen addition in premixed methane/air flames. *Int J Hydrog Energy* 32(13):2585–2592. <https://doi.org/10.1016/j.ijhydene.2006.11.033>
- Harvey J (1962) Some observations of the vortex breakdown phenomenon. *J Fluid Mech* 14(4):585–592
- Hawkes ER, Chen JH (2004) Direct numerical simulation of hydrogen-enriched lean premixed methane-air flames. *Combust Flame* 138(3):242–258. <https://doi.org/10.1016/j.combustflame.2004.04.010>
- Hoffmann S, Habisreuther P, Lenze B (1994) Development and assessment of correlations for predicting stability limits of swirling flames. *Chem Eng Process Process Intensif* 33(5):393–400. [https://doi.org/10.1016/0255-2701\(94\)02011-6](https://doi.org/10.1016/0255-2701(94)02011-6)
- Hong S, Shanbhogue SJ, Speth RL et al (2013) On the phase between pressure and heat release fluctuations for propane/hydrogen flames and its role in mode transitions. *Combust Flame* 160(12):2827–2842. <https://doi.org/10.1016/j.combustflame.2013.07.001>
- Hord J (1978) Is hydrogen a safe fuel? *Int J Hydrog Energy* 3(2):157–176. [https://doi.org/10.1016/0360-3199\(78\)90016-2](https://doi.org/10.1016/0360-3199(78)90016-2)
- Huang Y, Yang V (2009) Dynamics and stability of lean-premixed swirl-stabilized combustion. *Prog Energy Combust Sci* 35(4):293–364
- Janus MC, Richards GA, Yip MJ, et al (1997) Effects of ambient conditions and fuel composition on combustion stability. In: Turbo Expo: Power for Land, Sea, and Air, American Society of Mechanical Engineers, p V002T06A035. <https://doi.org/10.1115/97-GT-266>
- Juniper MP, Sujith RI (2018) Sensitivity and nonlinearity of thermoacoustic oscillations. *Annu Rev Fluid Mech* 50:661–689. <https://doi.org/10.1146/annurev-fluid-122316-045125>
- Kim HS, Arghode VK, Linck MB et al (2009) Hydrogen addition effects in a confined swirl-stabilized methane-air flame. *Int J Hydrog Energy* 34(2):1054–1062. <https://doi.org/10.1016/j.ijhydene.2008.10.034>
- Kushwaha A, Kasthuri P, Pawar SA, et al (2021) Dynamical characterization of thermoacoustic oscillations in a hydrogen-enriched partially premixed swirl-stabilized methane/air combustor. *J Eng Gas Turbines Power* 143(12)
- Lee T, Kim KT (2020) Combustion dynamics of lean fully-premixed hydrogen-air flames in a mesoscale multinozzle array. *Combust Flame* 218:234–246
- Liang H, Maxworthy T (2005) An experimental investigation of swirling jets. *J Fluid Mech* 525:115–159. <https://doi.org/10.1017/S0022112004002629>
- Lieuwen TC (2021) Unsteady combustor physics. Cambridge University Press
- Lieuwen TC, Yang V (2005) Combustion instabilities in gas turbine engines: operational experience, fundamental mechanisms, and modeling. American Institute of Aeronautics and Astronautics
- Lohrasbi S, Hammer R, Essl W et al (2021) A modification to extended proper orthogonal decomposition-based correlation analysis: the spatial consideration. *Int J Heat Mass Transf* 175:121065. <https://doi.org/10.1016/j.ijheatmasstransfer.2021.121065>
- Lumley JL (1967) The structure of inhomogeneous turbulent flows. Atmospheric turbulence and radio wave propagation pp 166–178
- Mandilas C, Ormsby M, Sheppard C et al (2007) Effects of hydrogen addition on laminar and turbulent premixed methane and iso-octane-air flames. *Proc Combust Inst* 31(1):1443–1450. <https://doi.org/10.1016/j.proci.2006.07.157>
- Moeck JP, Paschereit CO (2012) Nonlinear interactions of multiple linearly unstable thermoacoustic modes. *Int J Spray Combust Dyn* 4(1):1–27

- Mondal S, Pawar S, Sujith RI (2017) Synchronous behaviour of two interacting oscillatory systems undergoing quasiperiodic route to chaos. *Chaos: An Interdisc J Nonlinear Sci* 27(10):103119. <https://doi.org/10.1063/1.4991744>
- Nair V, Sujith RI (2014) Multifractality in combustion noise: predicting an impending combustion instability. *J Fluid Mech* 747:635–655. <https://doi.org/10.1017/jfm.2014.171>
- Nair V, Thampi G, Karuppusamy S et al (2013) Loss of chaos in combustion noise as a precursor of impending combustion instability. *Int J Spray Combust Dyn* 5(4):273–290. <https://doi.org/10.1260/1756-8277.5.4.273>
- Nakahara M, Kido H (2008) Study on the turbulent burning velocity of hydrogen mixtures including hydrocarbon. *AIAA J* 46(7):1569–1575. <https://doi.org/10.2514/1.23560>
- Nam J, Lee Y, Joo S et al (2019) Numerical analysis of the effect of the hydrogen composition on a partially premixed gas turbine combustor. *Int J Hydrog Energy* 44(12):6278–6286. <https://doi.org/10.1016/j.ijhydene.2019.01.066>
- Oberleithner K, Sieber M, Nayeri CN et al (2011) Three-dimensional coherent structures in a swirling jet undergoing vortex breakdown: stability analysis and empirical mode construction. *J Fluid Mech* 679:383–414. <https://doi.org/10.1017/jfm.2011.141>
- Oberleithner K, Terhaar S, Rukes L, et al (2013) Why nonuniform density suppresses the precessing vortex core. *J Engng Gas Turbines Pow* 135(12)
- Oberleithner K, Stöhr M, Im SH et al (2015) Formation and flame-induced suppression of the precessing vortex core in a swirl combustor: experiments and linear stability analysis. *Combust Flame* 162(8):3100–3114. <https://doi.org/10.1016/j.combustflame.2015.02.015>
- Pawar SA, Seshadri A, Unni VR et al (2017) Thermoacoustic instability as mutual synchronization between the acoustic field of the confinement and turbulent reactive flow. *J Fluid Mech* 827:664–693. <https://doi.org/10.1017/jfm.2017.438>
- Pignatelli F, Kim H, Subash A et al (2022) Pilot impact on turbulent premixed methane/air and hydrogen-enriched methane/air flames in a laboratory-scale gas turbine model combustor. *Int J Hydrog Energy* 47(60):25404–25417. <https://doi.org/10.1016/j.ijhydene.2022.05.282>
- Pikovsky A, Rosenblum M, Kurths J et al (2001) A universal concept in nonlinear sciences. *Self* 2:3
- Poinsot TJ, Trounev AC, Veynante DP et al (1987) Vortex-driven acoustically coupled combustion instabilities. *J Fluid Mech* 177:265–292. <https://doi.org/10.1017/S0022112087000958>
- Putnam AA (1971) Combustion-driven oscillations in industry. Elsevier Publishing Company
- Qadri UA, Mistry D, Juniper MP (2013) Structural sensitivity of spiral vortex breakdown. *J Fluid Mech* 720:558–581. <https://doi.org/10.1017/jfm.2013.34>
- Rashwan SS, Nemitallah MA, Habib MA (2016) Review on premixed combustion technology: stability, emission control, applications, and numerical case study. *Energy Fuels* 30(12):9981–10014. <https://doi.org/10.1021/acs.energyfuels.6b02386>
- Rayleigh JWS (1878) The explanation of certain acoustical phenomena. *Nature* 18(455):319–321. <https://doi.org/10.1038/018319a0>
- Reddy AP, Sujith R, Chakravarthy S (2006) Swirler flow field characteristics in a sudden expansion combustor geometry. *J Propul Power* 22(4):800–808. <https://doi.org/10.2514/1.15940>
- Rosenblum MG, Pikovsky AS, Kurths J (1996) Phase synchronization of chaotic oscillators. *Phys Rev Lett* 76(11):1804
- Schadow K, Gutmark E (1992) Combustion instability related to vortex shedding in dump combustors and their passive control. *Prog Energy Combust Sci* 18(2):117–132. [https://doi.org/10.1016/0360-1285\(92\)90020-2](https://doi.org/10.1016/0360-1285(92)90020-2)
- Schefer R (2003) Hydrogen enrichment for improved lean flame stability. *Int J Hydrog Energy* 28(10):1131–1141. [https://doi.org/10.1016/S0360-3199\(02\)00199-4](https://doi.org/10.1016/S0360-3199(02)00199-4)
- Schefer RW, Wicksall D, Agrawal A (2002) Combustion of hydrogen-enriched methane in a lean premixed swirl-stabilized burner. *Proc Combust Inst* 29(1):843–851. [https://doi.org/10.1016/S1540-7489\(02\)80108-0](https://doi.org/10.1016/S1540-7489(02)80108-0)
- Schmitt P, Poinsot T, Schuermans B et al (2007) Large-eddy simulation and experimental study of heat transfer, nitric oxide emissions and combustion instability in a swirled turbulent high-pressure burner. *J Fluid Mech* 570:17–46. <https://doi.org/10.1017/S0022112006003156>
- Shanbhogue SJ, Sanusi YS, Taamallah S et al (2016) Flame macrostructures, combustion instability and extinction strain scaling in swirl-stabilized premixed CH₄/H₂ combustion. *Combust Flame* 163:494–507. <https://doi.org/10.1016/j.combustflame.2015.10.026>
- Sieber M, Oliver Paschereit C, Oberleithner K (2017) Advanced identification of coherent structures in swirl-stabilized combustors. *J Eng Gas Turbines Power*. <https://doi.org/10.1115/1.4034261>
- Singh S, Roy A, Dhadphale JM, et al (2022) Mean-field synchronization model of turbulent thermoacoustic transitions. arXiv preprint [arXiv:2208.11550](https://arxiv.org/abs/2208.11550)
- Sirovich L (1987) Turbulence and the dynamics of coherent structures. I. coherent structures. *Q Appl Math* 45(3):561–571. <https://doi.org/10.1090/qam/910462>
- Sterling J, Zukoski EE (1987) Longitudinal mode combustion instabilities in a dump combustor. *AIAA*
- Stöhr M, Sadanandan R, Meier W (2011) Phase-resolved characterization of vortex-flame interaction in a turbulent swirl flame. *Exp Fluids* 51(4):1153–1167
- Strakey P, Sidwell T, Ontko J (2007) Investigation of the effects of hydrogen addition on lean extinction in a swirl stabilized combustor. *Proc Combust Inst* 31(2):3173–3180. <https://doi.org/10.1016/j.proci.2006.07.077>
- Sui J, Zhao D, Zhang B et al (2017) Experimental study of Rijke-type thermoacoustic instability by using proper orthogonal decomposition method. *Exp Therm Fluid Sci* 81:336–344. <https://doi.org/10.1016/j.expthermflusci.2016.10.026>
- Sujith RI, Pawar SA (2021) Thermoacoustic Instability: A Complex Systems Perspective. Springer Nature
- Syred N, Giles A, Lewis J et al (2014) Effect of inlet and outlet configurations on blow-off and flashback with premixed combustion for methane and a high hydrogen content fuel in a generic swirl burner. *Appl Energy* 116:288–296. <https://doi.org/10.1016/j.apenergy.2013.11.071>
- Taamallah S, LaBry ZA, Shanbhogue SJ et al (2015) Thermo-acoustic instabilities in lean premixed swirl-stabilized combustion and their link to acoustically coupled and decoupled flame macrostructures. *Proc Combust Inst* 35(3):3273–3282. <https://doi.org/10.1016/j.proci.2014.07.002>
- Taira K, Brunton SL, Dawson ST et al (2017) Modal analysis of fluid flows: an overview. *AIAA J* 55(12):4013–4041. <https://doi.org/10.2514/1.J056060>
- Tuncer O, Acharya S, Uhm J (2009) Dynamics, NO_x and flashback characteristics of confined premixed hydrogen-enriched methane flames. *Int J Hydrog Energy* 34(1):496–506. <https://doi.org/10.1016/j.ijhydene.2008.09.075>
- Wang P, Ma H, Liu Y (2018) Pod and extended-pod analysis of pressure fluctuations and vortex structures inside a steam turbine control valve. In: *Turbo Expo: Power for Land, Sea, and Air*, American Society of Mechanical Engineers, p V008T29A011
- Wang P, Ma H, Liu Y (2019) Proper orthogonal decomposition and extended-proper orthogonal decomposition analysis of pressure fluctuations and vortex structures inside a steam turbine control

- valve. *J Eng Gas Turbines Power*. <https://doi.org/10.1115/1.4040903>
- Wicksall D, Agrawal A, Schefer R et al (2005) The interaction of flame and flow field in a lean premixed swirl-stabilized combustor operated on H₂/CH₄/air. *Proc Combust Inst* 30(2):2875–2883. <https://doi.org/10.1016/j.proci.2004.07.021>
- Wilke C (1950) A viscosity equation for gas mixtures. *Chin J Chem Phys Chin* 18(4):517–519. <https://doi.org/10.1063/1.1747673>
- Xia H, Han W, Wei X et al (2022) Numerical investigation of boundary layer flashback of CH₄/H₂/air swirl flames under different thermal boundary conditions in a bluff-body swirl burner. *Proc Combust Inst*. <https://doi.org/10.1016/j.proci.2022.07.040>
- Zhang J, Ratner A (2019) Experimental study on the excitation of thermoacoustic instability of hydrogen-methane/air premixed flames under atmospheric and elevated pressure conditions. *Int J Hydrog Energy* 44(39):21324–21335. <https://doi.org/10.1016/j.ijhydene.2019.06.142>
- Zhang Q, Shanbhogue SJ, Shreekrishna, et al (2011) Strain characteristics near the flame attachment point in a swirling flow. *Combust Sci Technol* 183(7):665–685. <https://doi.org/10.1080/00102202.2010.537288>
- Zhang W, Wang J, Lin W et al (2020) Effect of differential diffusion on turbulent lean premixed hydrogen enriched flames through structure analysis. *Int J Hydrog Energy* 45(18):10920–10931. <https://doi.org/10.1016/j.ijhydene.2020.02.032>
- Zhen H, Cheung CS, Leung CW et al (2012) Effects of hydrogen concentration on the emission and heat transfer of a premixed lpg-hydrogen flame. *Int J Hydrog Energy* 37(7):6097–6105

Publisher's Note Springer Nature remains neutral with regard to jurisdictional claims in published maps and institutional affiliations.

Springer Nature or its licensor (e.g. a society or other partner) holds exclusive rights to this article under a publishing agreement with the author(s) or other rightsholder(s); author self-archiving of the accepted manuscript version of this article is solely governed by the terms of such publishing agreement and applicable law.